

## The Surface Expression of Semidiurnal Internal Tides near a Strong Source at Hawaii. Part I: Observations and Numerical Predictions\*

C. CHAVANNE, P. FLAMENT, G. CARTER, M. MERRIFIELD, AND D. LUTHER

*School of Ocean and Earth Science and Technology, University of Hawaii at Manoa, Honolulu, Hawaii*

E. ZARON

*Civil and Environmental Engineering, Portland State University, Portland, Oregon*

K.-W. GURGEL

*Institute of Oceanography, University of Hamburg, Hamburg, Germany*

(Manuscript received 21 January 2009, in final form 10 January 2010)

### ABSTRACT

Observations of semidiurnal currents from high-frequency radio Doppler current meters and moored acoustic Doppler current profilers (ADCPs) in the Kauai Channel, Hawaii, are described and compared with two primitive equation numerical models of the tides. The Kauai Channel, separating the islands of Oahu and Kauai, is a site of strong internal tide generation by the barotropic tides flowing over Kaena Ridge, the sub-surface extension of Oahu. The nature and impacts of internal tide generation in the Kauai Channel were intensively studied during the 2002–03 near-field component of the Hawaii Ocean Mixing Experiment.

Comparisons of observed coherent (i.e., phase locked to the astronomical forcing)  $M_2$  and  $S_2$  surface currents with model predictions show good agreement for the phases, indicating propagation of internal tides away from the ridge. Although the predicted  $M_2$  and  $S_2$  surface currents are similar (except for their magnitudes), as expected for internal waves at periods closer to each other (12.4 and 12 h, respectively) than to the inertial period (33 h), the observed  $M_2$  and  $S_2$  surface currents differ significantly. The  $S_2$  kinetic energy pattern resembles the predicted pattern. In contrast, the observed structure and magnitude of the more important  $M_2$  kinetic energy pattern differs significantly from the model predictions. The models predict a band of enhanced  $M_2$  surface kinetic energy 30–40 km from the ridge axis, corresponding to the first surface reflection of internal tide beams generated on the ridge flanks. The beams are clearly observed by the moored ADCPs, albeit with weaker amplitudes than predicted. Observations at the surface show an area of enhanced kinetic energy that is 10–20 km farther away from the ridge than predicted, with weaker magnitude. Observed  $M_2$  surface currents also exhibit apparent seasonal variability, with magnitudes weaker in spring 2003 than in fall 2002.

Complex-demodulated semidiurnal currents exhibit significant temporal variability in amplitude and phase, not only because of the interference between semidiurnal constituents (e.g., the spring–neap cycle) but also on shorter and irregular time scales. The result is that ~20% of semidiurnal energy is incoherent with astronomical forcing. Furthermore, the temporal variability is not spatially coherent; the spatial patterns of semidiurnal kinetic energy resemble those predicted by the numerical models during the strongest spring tides but differ from them at other times. As a result,  $M_2$  and  $S_2$  kinetic energy patterns phase locked to the astronomical forcing differ from each other. Some features of the observed spatial pattern and amplitude modulations can be qualitatively reproduced by a simple analytical model of the effects of homogeneous barotropic background currents on internal tide beams.

---

\* University of Hawaii at Manoa School of Ocean and Earth Science and Technology Contribution Number 7860.

---

Corresponding author address: Cédric Chavanne, School of Environmental Sciences, University of East Anglia, Norwich NR4 7TJ, United Kingdom.

E-mail: cedric.chavanne@ensta.org

DOI: 10.1175/2010JPO4222.1

## 1. Introduction

Tides are believed to provide a significant amount of the power required to maintain the abyssal stratification by in situ mechanical mixing (Munk and Wunsch 1998; St. Laurent and Simmons 2006). The pathways from the basin-scale barotropic (or surface) tides to the centimeter-scale mixing processes are not fully understood and not well parameterized in numerical models, a major concern for climate simulations (Wunsch and Ferrari 2004; Kuhlbrodt et al. 2007). Direct dissipation by bottom drag is negligible in the deep ocean, where loss of barotropic tidal energy is through conversion into baroclinic (or internal) tides at abrupt topography (Egbert and Ray 2000, 2001). High vertical modes rapidly dissipate (St. Laurent and Garrett 2002), contributing to enhanced diapycnal mixing observed near rough topography (Lueck and Mudge 1997; Polzin et al. 1997; Ledwell et al. 2000; St. Laurent and Nash 2004), whereas low vertical modes propagate over thousands of kilometers (Dushaw et al. 1995; Ray and Mitchum 1996, 1997; Cummins et al. 2001; Alford 2003; Alford et al. 2007; Alford and Zhao 2007), carrying much of the baroclinic tidal energy away from the generation sites and impairing our understanding of how and where diapycnal mixing occurs.

The Hawaii Ocean Mixing Experiment (HOME; Rudnick et al. 2003; Pinkel and Rudnick 2006) was designed to study tidal mixing and quantify the tidal energy budget along the Hawaiian Ridge, an isolated topographic feature in the central North Pacific. The  $M_2$  barotropic energy is estimated to be lost at a rate of 18–25 GW from the 2500-km ridge (Egbert and Ray 2001; Zaron and Egbert 2006a). A substantial fraction of this energy is transferred to internal tides. Estimates of internal tide energy fluxes from satellite altimeter observations of temporally and spatially coherent first-mode  $M_2$  internal tides vary: Ray and Cartwright (2001) obtain 6 GW, whereas Dushaw (2002) obtains only 2.6 GW over an area slightly smaller than that used by Ray and Cartwright (2001). Estimates from nonassimilative numerical simulations vary as well: Merrifield and Holloway (2002), using a regional 3D primitive equation model with 4-km horizontal resolution, obtain  $\sim 10$  GW of  $M_2$  baroclinic energy flux radiated away from the Hawaiian Ridge, of which 6 GW is carried by the first mode, a value consistent with the observational estimate of Ray and Cartwright (2001). However, using the same model over a smaller domain with horizontal resolution increased to 1 km, Carter et al. (2008) obtained a 20% increase in the barotropic-to-baroclinic conversion compared with that obtained using a 4-km-resolution simulation. The value, if any, to which these estimates would converge with further

increase in model resolution is not known, but these results suggest that more energy is converted from barotropic to baroclinic tides than estimated from altimeter observations.

However, comparing the baroclinic energy fluxes estimated from phase-locked observations with numerical predictions using time-independent stratification and no background currents is questionable. Temporally and spatially varying stratification associated with mesoscale currents has been shown to substantially impact the propagation of internal tides (Park and Watts 2006; Rainville and Pinkel 2006; Hosegood and van Haren 2006), and the resulting amplitude and phase modulation smears energy out of the phase-locked signals. Therefore, baroclinic energy fluxes estimated from phase-locked observations should be considered as lower bounds (Ray and Cartwright 2001; Dushaw 2002).

To provide information on the spatial and temporal variability of the mesoscale background through which internal tides propagate in the Kauai Channel, a “hot spot” for internal tide generation (Merrifield et al. 2001), two high-frequency radio (HFR) Doppler surface current meters were deployed on the west shore of Oahu and seven acoustic Doppler current profilers (ADCPs) were moored in the Kauai Channel during the HOME near-field observation program in 2002 and 2003. We compare phase-locked semidiurnal currents extracted from these observations with the predictions of two different numerical models. Both models compute the internal tide generation and propagation with realistic bathymetry and stratification in an ocean at rest, but they differ in their approach. One model [Princeton Ocean Model (POM); Carter et al. 2008] is nonlinear and uses a complex turbulent closure scheme, whereas the other [Primitive Equations Z-coordinate–Harmonic Analysis Tides (PEZHAT); Zaron and Egbert 2006b] is linear with simple weak downgradient diffusion. A companion paper (Zaron et al. 2009) presents a data-assimilative solution for PEZHAT to infer the nonlinear and dissipative dynamics from the HFR phase-locked  $M_2$  observations.

This paper is organized as follows: the experimental setting is described in section 2, and the numerical models are described and compared in section 3, to set the stage for the observations. Phase-locked semidiurnal currents are extracted from observed currents and compared with the numerical predictions in section 4. The observed currents are also complex demodulated to characterize the amplitude and phase variability of the semidiurnal currents in section 5. The results are discussed in section 6 and summarized in section 7. The instruments and data processing steps are described in appendix A, and HFR data are validated in appendix B.

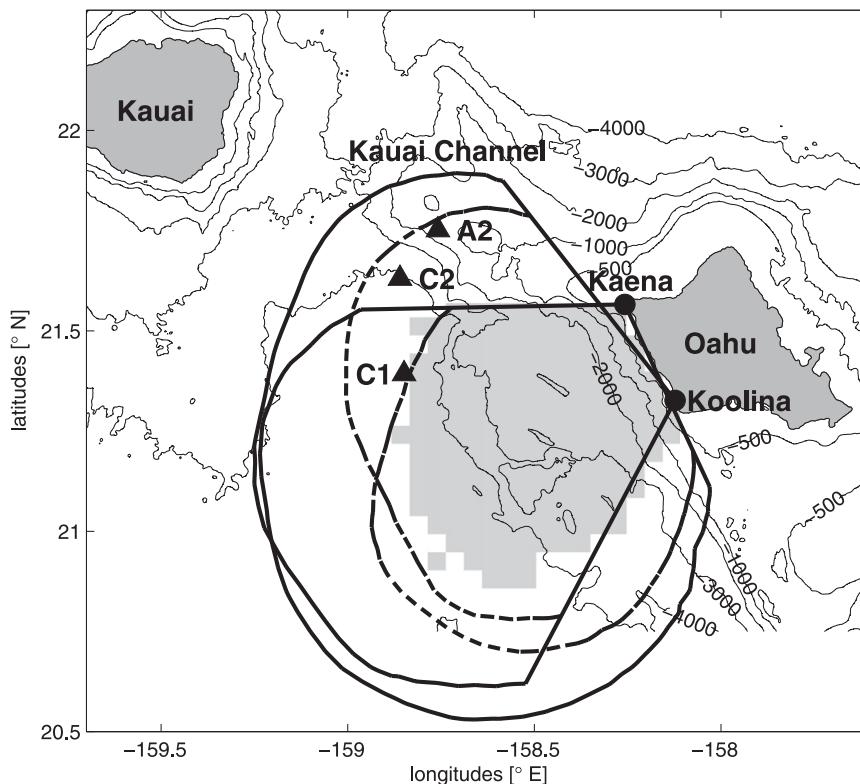


FIG. 1. Bathymetry (thin lines, from 150-m resolution data; Eakins et al. 2003) of the Kauai Channel, between the islands of Kauai and Oahu (shaded in dark gray). Here and in subsequent figures, isobaths are shown at 500, 1000, 2000, 3000, and 4000 m. Limits of 50% radial current return over the period from 12 Sep to 10 Nov 2002 are indicated for each HFR site (black bullets at Kaena and Ko Olina) for daytime (1600–0400 UTC, thick solid lines) and nighttime (0400–1600 UTC, thick dashed lines). The area of 50% vector current return is shaded in light gray. The locations of the moored ADCPs (C1, C2, and A2) are indicated by black triangles.

## 2. Experimental setting

Two 16-MHz HFRs were deployed along the west shore of Oahu, Hawaii (Fig. 1), from September 2002 to May 2003. They infer the radial component of surface currents (effective depth of  $\sim 1$  m; Stewart and Joy 1974) from the Doppler shift of radio waves Bragg scattered by surface gravity waves of half the electromagnetic wavelength, or 9.35 m at 16 MHz. At least two sites are required to construct vector currents. The northern site was at Kaena Point ( $21.57^{\circ}\text{N}$ ,  $158.26^{\circ}\text{W}$ ), on top of a cliff 360 m above mean sea level. The southern site was at Ko Olina ( $21.33^{\circ}\text{N}$ ,  $158.12^{\circ}\text{W}$ ), along the shore at sea level. The spatial resolution for radial currents was 1.2–1.5 km in range and  $7^{\circ}$ – $15^{\circ}$  in azimuth, and temporal resolution was 20–30 min. Vector currents were hourly mapped on a 5-km-resolution Cartesian grid. See appendix A for details.

Seven ADCPs were deployed upward looking in the Kauai Channel: two on mooring C1 ( $21.39^{\circ}\text{N}$ ,  $158.85^{\circ}\text{W}$ )

in 4700-m water depth, two on mooring C2 ( $21.63^{\circ}\text{N}$ ,  $158.86^{\circ}\text{W}$ ) in 4010-m water depth, and three on mooring A2 ( $21.75^{\circ}\text{N}$ ,  $158.76^{\circ}\text{W}$ ; Boyd et al. 2005) in 1330-m water depth (see Fig. 1 for their locations). ADCPs covered depths between 12 and 80 m with 4-m vertical resolution at each mooring and 168–720 m at C1, 200–720 m at C2, and 160–1296 m at A2, with 8-m vertical resolution. Currents were hourly averaged.

Temporal coverages of the instruments are shown in Fig. 2. Failures occurred at both HFR sites because of electrical power loss, cables damaged by surf run up at Ko Olina and by high winds at Kaena, and intermittent radio interferences. Data were lost for periods of a few days to 2 months at Kaena. Therefore, two 59-day periods (corresponding to four spring–neap cycles each) of almost uninterrupted coverage were selected for analysis: 11 September–9 November 2002 (fall 2002) and 3 March–1 May 2003 (spring 2003).

Rotary spectra of the surface currents (see Fig. 2 of Chavanne et al. 2010b, hereafter CFG) are red, with the

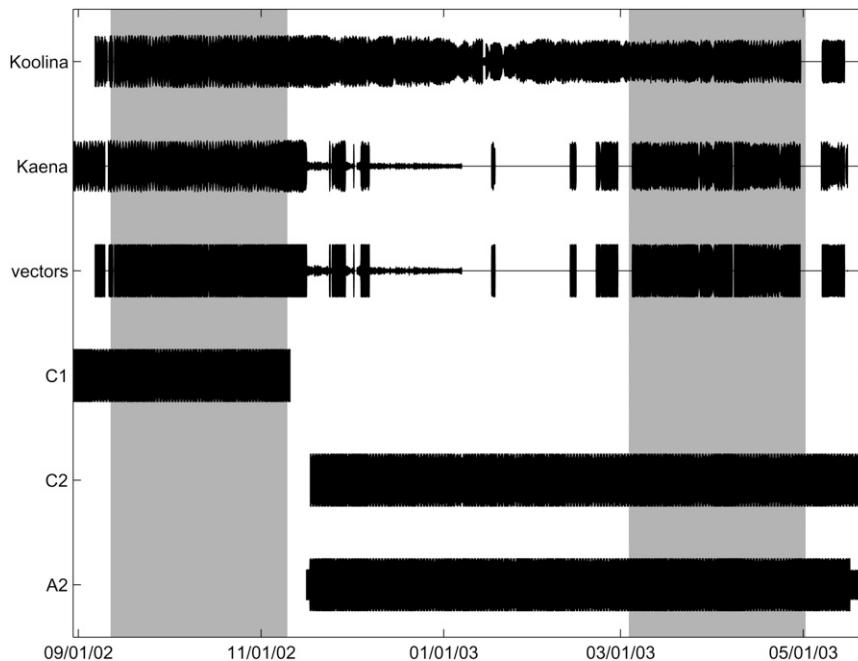


FIG. 2. Temporal coverage of radial currents from each HFR (Ko Olina and Kaena), the resulting vector currents (vectors), and currents from the moored ADCPs (C1, C2, and A2). The line thickness corresponds to the relative percentage of spatial coverage. The two 59-day periods selected in this study are shaded in gray: 12 Sep–10 Nov 2002 (fall 2002) and 3 Mar–1 May 2003 (spring 2003).

maximum energy at periods longer than 15 days. These low-frequency currents are described by Chavanne et al. (2010a, hereafter Part II), Chavanne et al. (2010, manuscript submitted to *J. Phys. Oceanogr.*), and CFG. The next strongest energy is in the semidiurnal tidal band, whereas the diurnal energy is an order of magnitude smaller with barely defined peaks. Higher harmonics, such as  $M_3$  and  $M_4$ , which may be generated by the nonlinear interaction between the incident and reflected beams at the surface (Lamb 2004), are distinguishable but weak. We focus here on the semidiurnal frequencies.

### 3. Numerical models

Two 3D stratified numerical models of the tides are used to set the stage for the observations. Both models compare reasonably well with altimetry and moored ADCPs (Zaron et al. 2009; Carter et al. 2008).

#### a. Description

PEZHAT (Zaron and Egbert 2006b) is a primitive equation model based on the Geophysical Fluid Dynamics Laboratory (GFDL) Modular Ocean Model (MOM3; Pacanowski and Griffies 1999) and a set of modules to implement the astronomical tidal forcing,

open boundary conditions, and harmonic analysis of the solutions. In the present application, PEZHAT is configured as a solver for the primitive equations linearized around a horizontally uniform background state, with a horizontal resolution of 2 km in the Kauai Channel (but decreasing toward the edges of the model domain) and 60 vertical levels with variable resolution, ranging from 30 m near the surface to 500 m in the deep ocean. It is forced by the normal component of the  $M_2$  barotropic (i.e., depth averaged) transport on open boundaries, inferred from a larger-scale data-assimilating barotropic tide model (Zaron and Egbert 2006a) and by astronomical body forcing, which includes corrections for self-attraction and solid-earth loading (Zaron et al. 2009). The baroclinic (i.e., deviations from depth average) velocities and isopycnal displacements are damped by Laplacian friction within an absorbing layer of width 225 km, which prevents internal waves from being reflected by the computational boundaries.

The second model, POM (Carter et al. 2008), is a nonlinear primitive equation model with a second moment turbulent closure submodel (Mellor and Yamada 2.5 level) and terrain-following ( $\sigma$ ) vertical coordinates. It has a horizontal resolution of  $0.01^\circ$  ( $\sim 1$  km) and 61  $\sigma$  levels spaced evenly in the vertical. It is forced by  $M_2$  elevation and barotropic velocity on open boundaries,

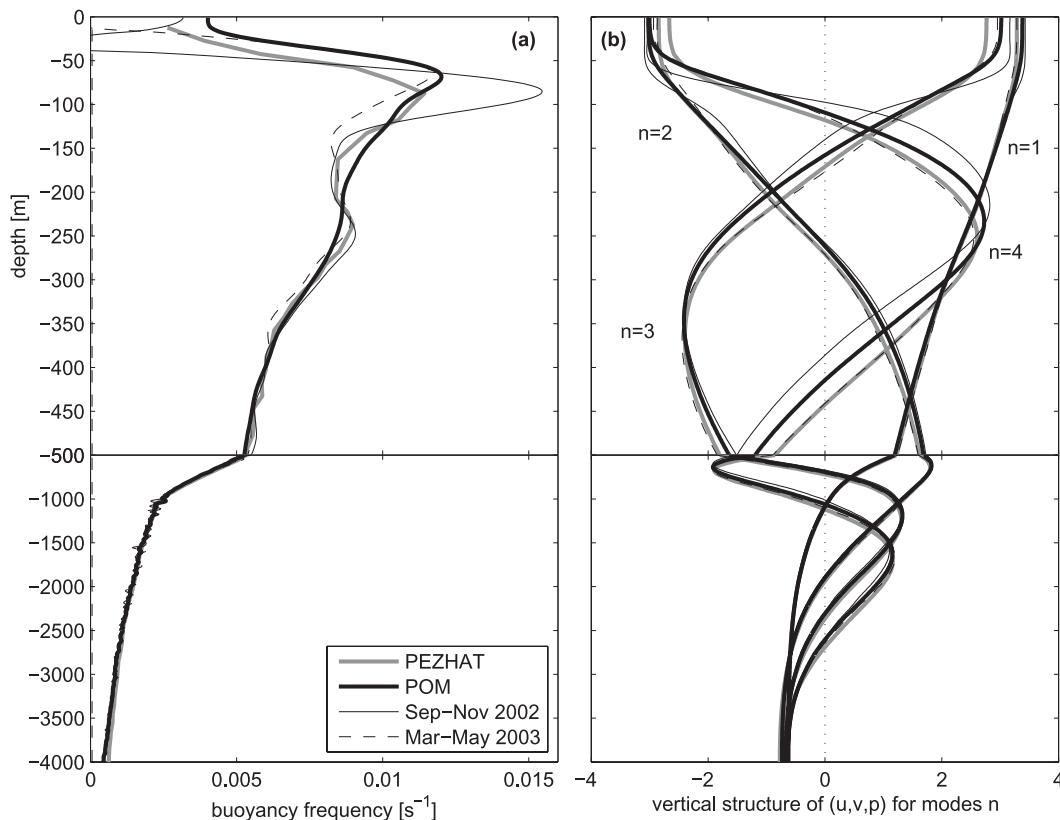


FIG. 3. (a) Buoyancy frequency ( $s^{-1}$ ) used in PEZHAT (thick gray line) and POM (thick black line) and averaged for September–November 2002 (thin solid line) and March–May 2003 (thin dashed line) from temperature and salinity observations at a station  $\sim 100$  km north of Oahu. (b) Vertical structures for  $u, v, p$  for the first 4 vertical modes, computed using the stratification profiles shown in (a) and assuming a bottom depth of 4000 m. The mode amplitudes were normalized to give vertical-mean-squared values of 1. Modes 1 and 3 are shown with positive values at the surface, whereas modes 2 and 4 are shown with negative values for clarity. Note the change in depth scale at 500 m.

inferred from the Hawaii region TPXO6.2 inverse model (Egbert and Erofeeva 2002), without body forcing. The baroclinic velocities and isopycnal displacements are relaxed to zero over a 10-cell-wide region, which prevents baroclinic energy from being reflected by the computational boundaries.

The simulation domains encompass the main Hawaiian Islands, excluding the Island of Hawaii, which is not associated with large baroclinic energy fluxes (Merrifield and Holloway 2002). The bathymetry is derived from multibeam sonar data (Eakins et al. 2003) smoothed and gridded to the model resolutions. The stratification is from temperature and salinity observations at Station ALOHA ( $22.75^{\circ}N, 158^{\circ}W$ ; Karl and Lukas 1996), located  $\sim 100$  km north of Oahu, averaged over 9 months (September 2002–May 2003) for PEZHAT and 10 yr for POM. The stratification profiles differ only slightly (mostly in the upper 300 m), with negligible effects on the lower vertical modes (Fig. 3): the surface values vary by less than 8% for the

first three modes. Other relevant model parameters are listed in Table 1.

*b. Results and comparisons*

The  $M_2$  kinetic energy and phase of the barotropic and surface baroclinic currents for both models are shown in Figs. 4 and 5. Phase is defined as the lag of the maximum  $M_2$  current, along the northern semimajor axis, with respect to the phase of the  $M_2$  contribution to the astronomical potential at  $0^{\circ}E$ .

The  $M_2$  internal tides are generated as the barotropic tide encounters the Hawaiian Ridge, propagating almost perpendicular to the ridge axis from the northeast (Larsen 1977). The elongated structure of the ridge forces the barotropic currents to flow over topography rather than around it (Fig. 4, top), inducing vertical velocities that advect isopycnals up and down along the ridge flanks. A resonance occurs when the topographic slope in the direction of the barotropic currents is equal to the internal

TABLE 1. Model parameters: horizontal resolution  $\Delta x$ ; vertical resolution  $\Delta z$ ; vertical viscosity and diffusivity,  $A_V$  and  $K_V$ ; horizontal viscosity and diffusivity,  $A_H$  and  $K_H$ ; time of model integration  $T$ ; time at the end of model integration used for harmonic analysis  $T_{HA}$ .

Parameter	PEZHAT	POM
$\Delta x$	2 km	$\sim 1$ km (0.01°)
$\Delta z$	60 $z$ levels unevenly spaced 30 m near the surface to 500 m at 4000 m	61 $\sigma$ levels evenly spaced
$A_V$	$5 \times 10^{-4} \text{ m}^2 \text{ s}^{-1}$	Mellor–Yamada 2.5
$K_V$	$0.5 \times 10^{-4} \text{ m}^2 \text{ s}^{-1}$	0
$A_H$	$12 \text{ m}^2 \text{ s}^{-1}$	Smagorinsky
$K_H$	$12 \text{ m}^2 \text{ s}^{-1}$	0
$T$	14 $M_2$ periods	18 $M_2$ periods
$T_{HA}$	3 $M_2$ periods	6 $M_2$ periods

tide characteristic slope (critical slope). At these locations, the baroclinic energy is focused into beams radiating up and down the water column along the characteristics, reflecting subsequently off the sea surface and bottom (Merrifield and Holloway 2002). This is illustrated in the vertical sections of baroclinic  $M_2$  kinetic energy (Fig. 6) and phase (Fig. 7) predicted by POM across the ridge.

Beams of enhanced kinetic energy emanate from critical slopes on both sides of the ridge crests and propagate upward before reflecting from the sea surface (Fig. 6). Phases are almost constant along the beams and vary rapidly in the cross-beam directions (Fig. 7), consistent with internal wave packets with group velocities parallel to the beams and phase velocities normal to the group velocities. The depths of the beams at the mooring locations differ by less than 100 m between both model predictions, except for the beam near the bottom at A2, where the model predictions differ by 270 m. Because the maximum energy of the deepest beam at A2 is at the bottom in both models, the difference in depth comes from the different resolutions used. Baroclinic currents are generally stronger in PEZHAT than in POM, especially along the beams. At A2, where three beams can be identified, vertically integrated baroclinic kinetic energy is twice as strong in PEZHAT as in POM.

The surface reflection areas are clearly visible in Fig. 4 (bottom) as arcs of enhanced surface baroclinic currents on both sides of the ridge  $\sim 30$ – $40$  km from the ridge axis. The phase of the surface baroclinic currents (Fig. 5, bottom) shows the propagation of the internal tides away from the ridge. Interference patterns with other generation areas are found south and north of Kauai and Oahu. In contrast, the barotropic phases vary over much larger scales, except around the islands where abrupt

phase changes are found (Fig. 5, top). The barotropic currents are less than  $5 \text{ cm s}^{-1}$  in deep water but can reach over  $30 \text{ cm s}^{-1}$  over the shallowest parts of the ridge (Fig. 4, top).

The barotropic current patterns are similar in both models, but barotropic kinetic energy volume averaged over  $21^\circ$ – $22.5^\circ\text{N}$ ,  $159.5^\circ$ – $158^\circ\text{W}$  (dashed box in Fig. 4a), to avoid the absorbing layer in PEZHAT, is 1.36 times stronger in PEZHAT than in POM. This can be attributed to the lack of body forcing in POM: body forcing in PEZHAT over the same volume amounts to 0.45 GW, or 35% of the 1.30 GW provided by the boundary forcing (the only forcing used in POM). Surface baroclinic current patterns show stronger differences, being weaker in POM in the surface reflection areas on each side of the Kauai Channel but weaker in PEZHAT south of Kauai (Fig. 4, bottom), in the surface reflection area of internal tides generated between Kauai and Niihau (the small island west of Kauai). This area lies in the absorbing layer in PEZHAT, so the internal tides are damped by the increased viscosity and their generation is less well resolved by the decreased horizontal resolution. Surface baroclinic kinetic energy spatially averaged over the rectangle shown in Fig. 4a is 1.66 times stronger in PEZHAT than in POM. Although baroclinic energies should be volume averaged to be properly compared, spatial averages at the surface are reported here to compare with surface observations from the HFRs in the next section.

#### 4. Model and observation comparisons

HFR and ADCP phase-locked tidal currents were extracted over each 59-day period, during which both types of instruments recorded data almost continuously (Fig. 2). Six tidal constituents ( $M_2$ ,  $S_2$ ,  $N_2$ ,  $K_1$ ,  $O_1$ , and  $Q_1$ ) were least squares fitted to high-pass-filtered observations, and uncertainties were estimated by a bootstrap technique (see appendix A).

Figure 8 shows the total (barotropic plus baroclinic)  $M_2$  surface current ellipses and phases at mooring C1. The kinetic energy observed at the surface by the HFRs is 1.7 times weaker than that observed by the ADCP at 12-m depth, and their inclination angles differ by  $22^\circ$ , whereas phases differ by only  $7^\circ$ . Both models overestimate the major axis amplitude at C1 but predict phases more accurately. Differences between the observations could be attributed in part to the different volumes sampled by each instrument, but the strong geometrical dilution of precision (GDOP; see appendix A) in the HFR vector currents near C1 is a significant source of noise. To eliminate the GDOP-induced noise amplification, tidal analysis was also performed on the radial currents measured by each HFR and on the projections of currents

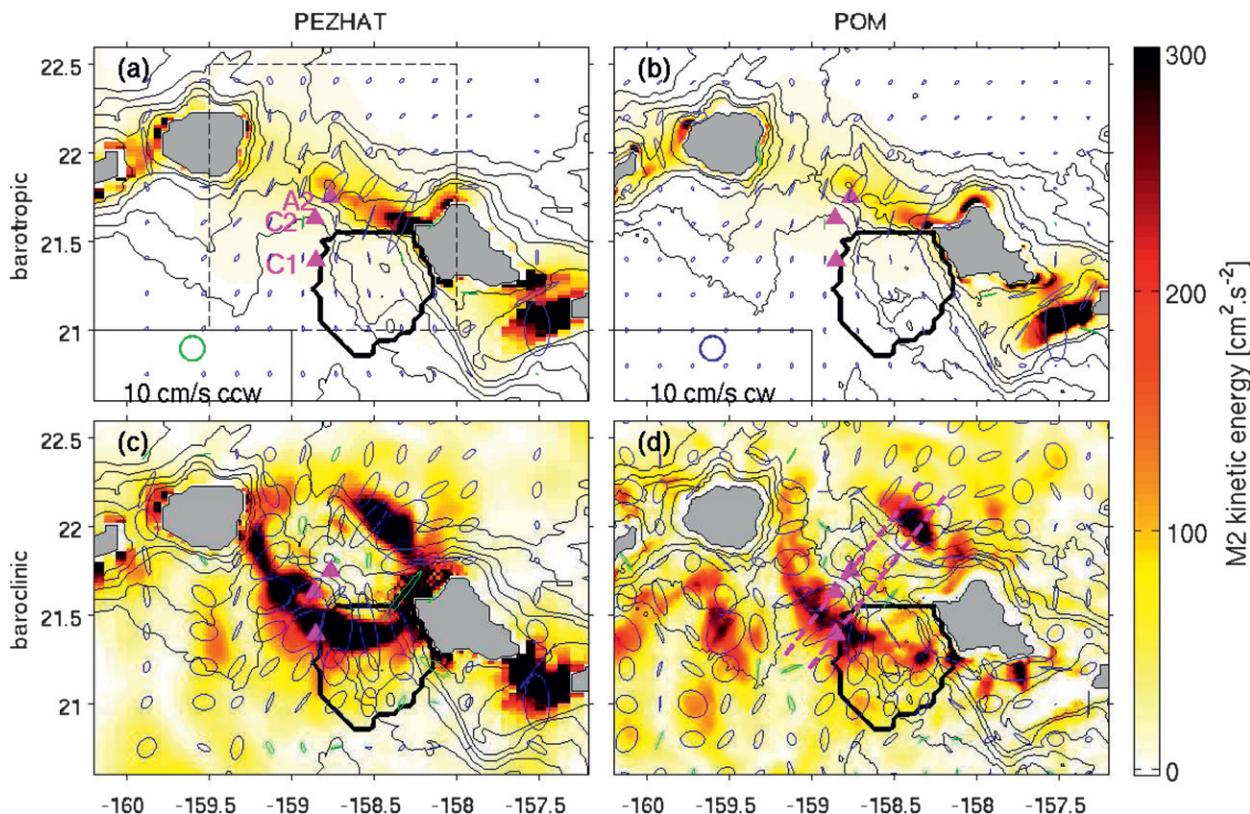


FIG. 4. The  $M_2$  kinetic energy and ellipses (green is counterclockwise and blue is clockwise) of the (top) barotropic and (bottom) surface baroclinic currents for (left) PEZHAT and (right) POM. The 50% data return area for the HFRs during fall 2002 is delimited by black thick lines, and the mooring positions are indicated by purple triangles. (a) The dashed black rectangle indicates the area over which kinetic energies are averaged for model comparisons. (d) The dashed purple lines indicate the locations of the vertical transects shown in Fig. 6. Bathymetry is from each model and isobaths are shown at 500, 1000, 2000, 3000, and 4000 m. Ellipses are shown every 10 grid points in longitude and latitude for PEZHAT (note the decrease of horizontal resolution in the absorbing layer toward the edges of the domain) and every 20 points for POM.

observed by the ADCP at 12-m depth onto the directions between C1 and the HFR sites. Figure 9 (top) shows the resulting amplitudes and phases (defined here as the lag of the maximum radial current away from the HFR site with respect to the phase of the  $M_2$  contribution to the astronomical potential at  $0^\circ$  longitude), along with those predicted by the models. Observed amplitudes in these directions are not significantly different from each other, whereas phases are. Both models overestimate amplitudes in these directions. For completeness, similar comparisons are shown at moorings C2 and A2 (Fig. 9, bottom). There, observed amplitudes are weak and neither observed amplitudes nor phases differ significantly, whereas predicted amplitudes are again overestimated.

The spatial patterns of phase-locked  $M_2$  surface currents are shown in Figs. 10 and 11. Although the total currents (barotropic plus baroclinic) are shown, the numerical predictions indicate that they are dominated by the baroclinic contribution over the observational domain (Figs. 4, 5). Strikingly, the areas of enhanced energy,

corresponding to the surface reflection of internal tide beams in the numerical predictions, have a quite different structure in the observations: they extend westward from Kaena Point, as predicted, but bend southward farther away from the ridge axis, peaking locally around  $(21.15^\circ\text{N}, 158.55^\circ\text{W})$ ,  $\sim 50$  km from the ridge axis, 10–20 km farther away than predicted. Spatial patterns and amplitudes vary seasonally, with the phase-locked  $M_2$  surface currents being weaker in spring 2003 than in fall 2002. Spatially averaged kinetic energy ratios between observations and numerical predictions are given in Table 2. Phases, on the other hand, show better agreement between observations and numerical predictions than amplitudes (Fig. 11). In the western half of the observational domain,  $M_2$  tides propagate to the southwest, normal to isobaths, whereas they propagate to the southeast in the eastern half, along isobaths.

Observations of the vertical structure of phase-locked baroclinic  $M_2$  currents from moored ADCPs are shown in Figs. 6 and 7. ADCPs covered almost the whole water

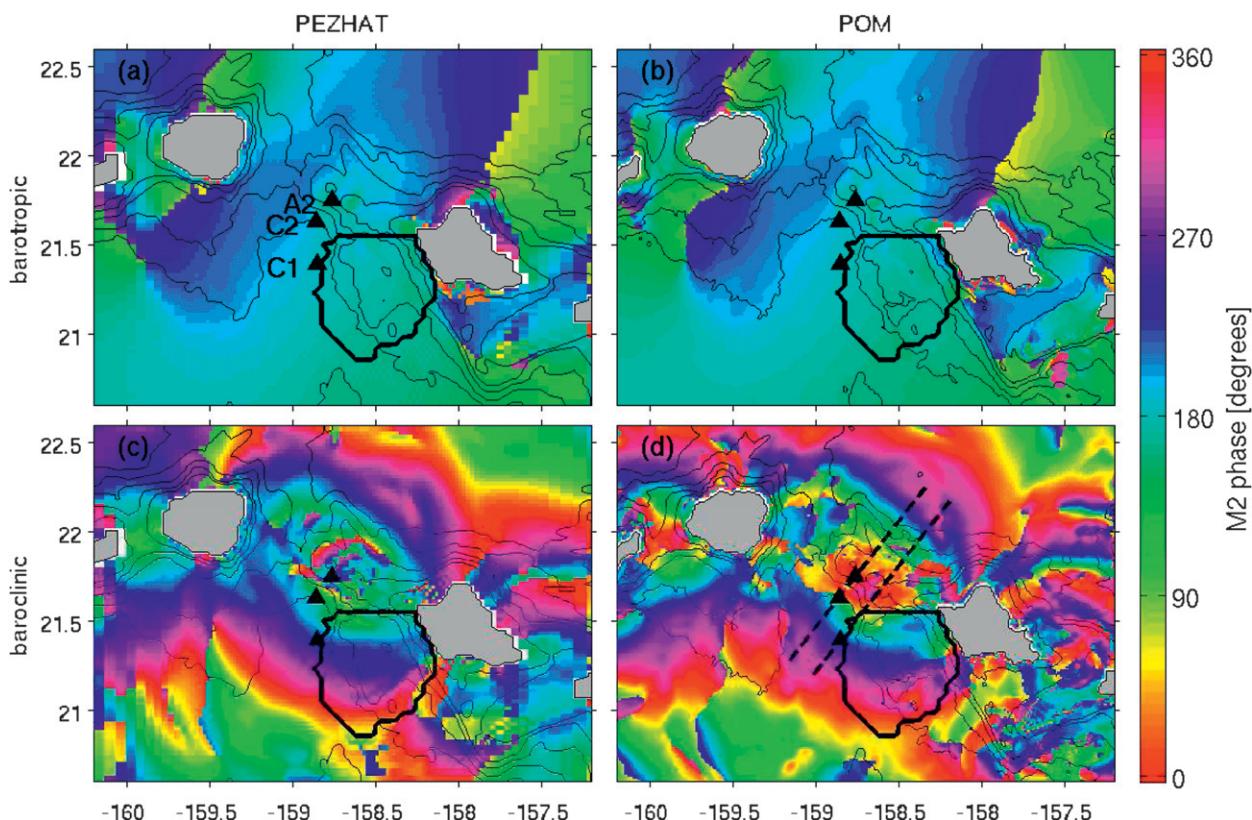


FIG. 5. The  $M_2$  phase of the (top) barotropic and (bottom) surface baroclinic currents for (a),(c) PEZHAT and (b),(d) POM. The 50% data return area for the HFRs during fall 2002 is delimited by black thick lines, and the mooring positions are indicated by black triangles. (d) The dashed black lines indicate the locations of the vertical transects shown in Fig. 7. Bathymetry is from each model and isobaths are shown at 500, 1000, 2000, 3000, and 4000 m.

column at A2, so baroclinic currents were computed by subtracting depth-averaged currents. At C1 and C2, ADCPs only covered a small portion of the water column, so barotropic currents from POM were subtracted to obtain baroclinic currents. As C1 and C2 were moored in deep water, barotropic currents are weak and rather well predicted by numerical models. The kinetic energy intensification and rapid phase changes associated with the internal tide beams in the numerical predictions are confirmed by observations. For example, three subsurface local intensifications are observed at A2 around 230 m, 650 m, and just above the bottom at 1290 m, associated with large vertical phase gradients and close to those predicted by POM. However, the observed amplitudes of the beams are weaker than predicted. As a result, vertically integrated kinetic energy observed at A2 is twice as weak as predicted by POM and almost 5 times weaker than predicted by PEZHAT. C1 and C2 were located near predicted areas of surface reflections of beams (Figs. 4, 6), but observed amplitudes at C1 are weaker than predicted in the top 100 m and the shallowest beam at C2 is not observed.

Finally, the predicted and observed patterns of surface  $S_2$  currents are compared in Fig. 12. For this constituent, predictions are available only from POM. The predicted  $S_2$  patterns are similar to the predicted  $M_2$  patterns (cf. Figs. 12e,f with Figs. 10d, 11d, respectively), with weaker amplitudes. This is expected for internal waves at periods closer to each other (12 and 12.4 h, respectively) than to the inertial period (33 h). In contrast, the observed  $S_2$  surface kinetic energy pattern is quite different from the observed  $M_2$  pattern (cf. Figs. 12a,c with Figs. 10a,b, respectively). The former displays areas of enhanced energy corresponding to the predicted surface reflection of  $S_2$  beams. Seasonal variations are much less pronounced than for  $M_2$ , with the area-integrated kinetic energy being similar in fall 2002 and spring 2003 (Table 2).

## 5. Observed amplitude and phase modulations

Predicted and observed phase-locked  $M_2$  currents have similar phases, but their kinetic energy patterns and magnitudes differ. These discrepancies cannot be attributed to

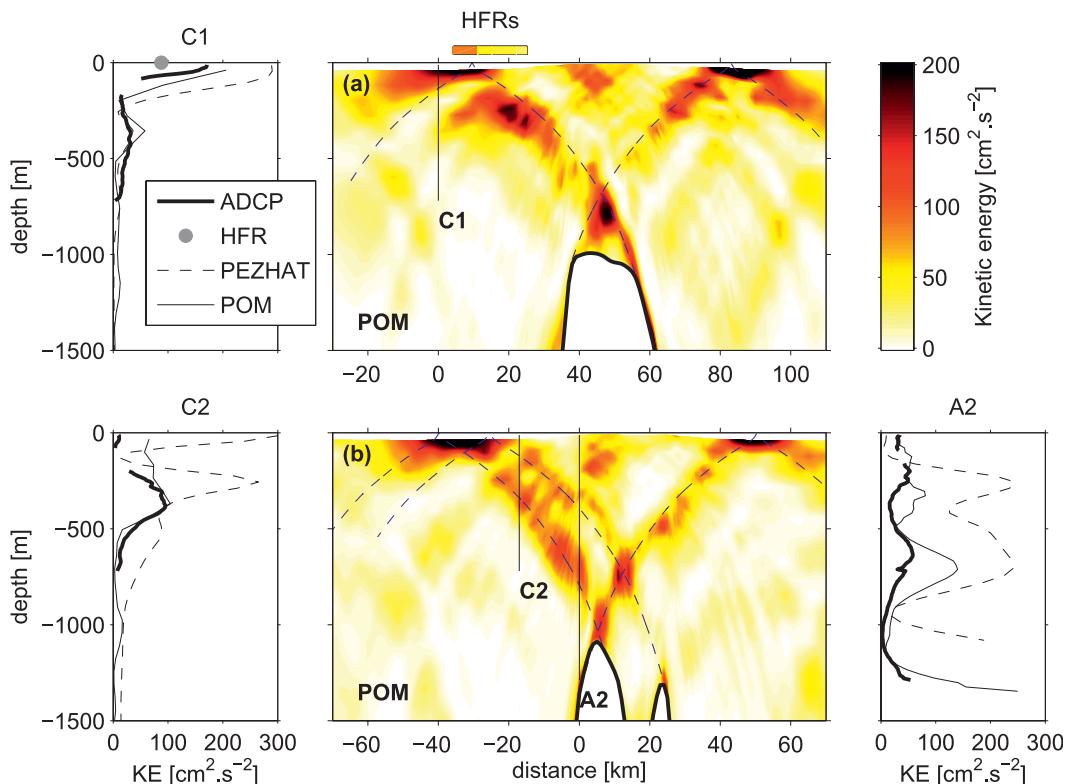


FIG. 6. Vertical structure of baroclinic  $M_2$  horizontal kinetic energy predicted by POM, along the transects going through (a) C1 and (b) C2–A2 (see Fig. 4d for the transect locations). HFR observations at grid points less than 5 km away from the transect going through C1 are shown above (a). Vertical lines indicate the locations of the moorings. Dashed lines indicate  $M_2$  characteristics originating at critical slopes for the model topography (thick black lines) and stratification. Vertical profiles at the moorings of ADCP observations (thick lines) and PEZHAT (thin dashed lines) and POM (thin solid lines) predictions are shown on the sides. The HFR observation at the grid point closest to C1 is indicated by a gray bullet at the surface. Barotropic currents predicted by POM were subtracted from HFR and ADCP observations, except at A2, where depth-averaged observed currents were subtracted from ADCP observations.

deficiencies of a particular model, because both models predict patterns that are more similar to each other than to the observations. The discrepancies must be due to physics missing in both models. A possible candidate is the lack of background currents and variable stratification in the models, which assume that internal tides propagate in an ocean at rest. In reality, mean currents flow along the Hawaiian Ridge on both sides, and sub-inertial variability is dominated by energetic mesoscale and submesoscale currents (Patzert 1969; Lumpkin 1998; Qiu et al. 1997; Flament et al. 2001; CFG; Chavanne et al. 2010, manuscript submitted to *J. Phys. Oceanogr.*).

Spatial variations in stratification associated with mesoscale currents in thermal wind balance, combined with Doppler shifting by the currents, modify the propagation paths and amplitude by refracting the internal tides (Rainville and Pinkel 2006; Park and Watts 2006). The resulting modification in travel time from the generation to the measurement locations modulates the phase of the

observed signal (Chiswell 2002; Alford et al. 2006). Phase and amplitude modulations lead to a leaking of energy into neighboring frequencies around the tidal frequencies (incoherent energy), hence decreasing the amount of coherent energy given by the harmonic analysis over periods of time longer than the modulation time scales (Colosi and Munk 2006).

To investigate the amplitude and phase modulations of the internal tides, we perform a complex demodulation analysis. The method is illustrated for the 12-m depth bin of the upper ADCP moored at C1 (Fig. 13) and the HFR grid point closest to C1 (Fig. 14). The observed currents (Figs. 13a, 14a, thin curves) are low-pass filtered (thick curves) to obtain residual high-pass-filtered currents ( $u'$ ,  $v'$ ) (Figs. 13b, 14b, black curves). The length of the demodulation window must be sufficient to robustly extract semidiurnal signals in the presence of noise and missing data but should not exceed the characteristic time scales of the mesoscale variability.

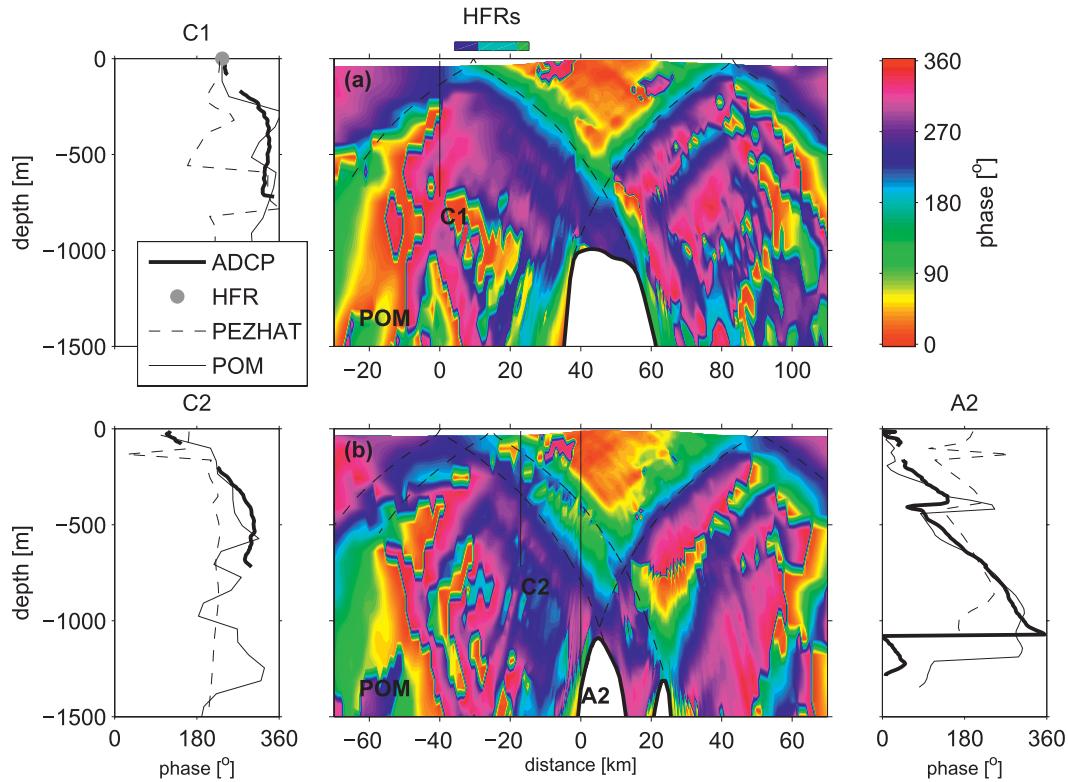


FIG. 7. As in Fig. 6, but for phase.

Eulerian integral time scales computed from the sub-inertial HFR currents vary over the observational domain between 4 and 15 days during fall 2002 and between 3 and 8 days during spring 2003. We therefore chose a window length of 4 days and move the window at daily time steps. The  $M_2$  and  $K_1$  tides are extracted over each 4-day segment by least squares fit, and uncertainties are estimated by a bootstrap technique (see appendix A). This procedure is suitable for data with missing observations (e.g., Fig. 14a). We obtain a time series of semi-diurnal amplitude,  $(u'_a, v'_a)$  and phase,  $(u'_p, v'_p)$ , for the zonal and meridional current components, from which ellipse parameters such as major axis amplitude (Figs. 13c, 14c, black curves) and phase (Figs. 13d, 14d, black curves) can be computed (e.g., Foreman 1978).

Because of the 4-day analysis window, it is not possible to separate  $M_2$  from the other semi-diurnal constituents, and the demodulated amplitudes and phases for  $M_2$  will display variations caused by interferences with the other semi-diurnal constituents. These modulations can be computed from the phase-locked tidal currents extracted by least squares fits over the 59-day records (Figs. 13b, 14b, red curves) as follows: Suppose we have a superposition of  $N$  different tidal constituents, with frequencies  $\omega_j$  ( $j = 1, \dots, N$ ), that we want to express as a single tidal constituent of frequency  $\omega_1$  (here  $\omega_1 = \omega_{M_2}$ ),

with a variable amplitude and phase. The zonal component of phase-locked tidal current  $\tilde{u}$  is given by

$$\tilde{u}(t) = \sum_{j=1}^N \tilde{u}_{aj} e^{i(\omega_j t + \tilde{u}_{pj})} = \tilde{u}_{0a}(t) e^{i[\omega_1 t + \tilde{u}_{0p}(t)]}, \quad (1)$$

where the variable amplitude is given by

$$\tilde{u}_{0a}(t) = (\tilde{u}\tilde{u}^*)^{1/2} = \left( \sum_{j=1}^N \sum_{k=1}^N \tilde{u}_{aj} \tilde{u}_{ak} e^{i[(\omega_j - \omega_k)t + \tilde{u}_{pj} - \tilde{u}_{pk}]} \right)^{1/2} \quad (2)$$

and the phase is given by

$$\tilde{u}_{0p}(t) = \arctan \left[ \frac{\sum_{j=1}^N \tilde{u}_{aj} \sin(\omega_j t + \tilde{u}_{pj})}{\sum_{j=1}^N \tilde{u}_{aj} \cos(\omega_j t + \tilde{u}_{pj})} \right] - \omega_1 t. \quad (3)$$

The same can be done for the meridional component  $\tilde{v}$  to obtain the variable amplitude  $\tilde{v}_{0a}$  and phase  $\tilde{v}_{0p}$ , from which ellipse parameters such as major axis amplitude (Figs. 13c, 14c, dashed blue curves) and phase (Figs. 13d, 14d, dashed blue curves) can be computed. To

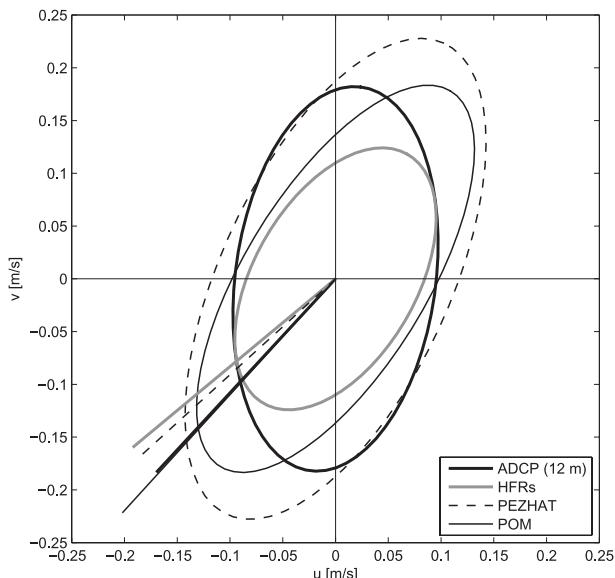


FIG. 8. Total (barotropic plus baroclinic)  $M_2$  surface current ellipses at C1 from the 12-m depth bin of the ADCP (thick solid line) and the HFR grid point closest to C1 (thick gray line) and from PEZHAT (thin dashed line) and POM (thin solid line) predictions. Phases are represented by the angle (counterclockwise from the abscissa) of the straight lines.

validate the complex-demodulation technique, we also apply it to the phase-locked tidal currents,  $(\tilde{u}, \tilde{v})$ , to obtain a time series of semidiurnal amplitude,  $(\tilde{u}_a, \tilde{v}_a)$ , and phase,  $(\tilde{u}_p, \tilde{v}_p)$ , from which ellipse parameters such as major axis amplitude (Figs. 13c, 14c, red curves) and phase (Figs. 13d, 14d, red curves) can be computed. The results compare well with those obtained from  $(\tilde{u}_{0a}, \tilde{v}_{0a})$  and  $(\tilde{u}_{0p}, \tilde{v}_{0p})$  (dashed blue curves).

Variability of complex-demodulated major axis amplitude and phase of high-pass-filtered currents (Figs. 13c,d, 14c,d, black curves) are dominated by interferences between the semidiurnal constituents (spring–neap cycle and 28-day modulations), captured by the complex-demodulated major axis amplitude and phase of phase-locked tidal currents (dashed blue or red curves). However, part of the observed variability cannot be attributed to these interferences: the parameters estimated from the high-pass-filtered currents sometimes depart significantly (at 95% confidence level) from those estimated from the phase-locked tidal currents. A striking example is the intensification of semidiurnal currents during 24–30 September, 2–8 days after the spring tide occurred in the phase-locked currents on 22 September, both for the ADCP and HFR observations. There is also a significant phase offset of  $\sim 25^\circ$  during this period between the high-pass-filtered and phase-locked semidiurnal currents observed by the ADCP. No such phase shift is consistently observed by the HFRs during the same

period, but phases are less robust for the HFR observations near C1 because of the large amount of missing data. Nevertheless, both instruments measure similar amplitude and phase modulations of the semidiurnal currents over the 59-day records.

The spatial structure of complex-demodulated semidiurnal kinetic energy of high-pass-filtered currents on 27 September is shown in Fig. 15a, with the subinertial currents superimposed. Energy is locally enhanced at and near C1, which is located near the maximum azimuthal currents associated with a mesoscale cyclone (only partly captured by the HFRs). Another area of local energy enhancement is located near the maximum azimuthal currents of the eddy on its southern edge, near  $(21.0^\circ\text{N}, 158.75^\circ\text{W})$ . This spatial pattern does not resemble the pattern that would be obtained from a superposition of  $M_2$  and  $S_2$  internal tides predicted by POM, which would resemble either the  $M_2$  (Fig. 10d) or  $S_2$  (Fig. 12e) pattern, given their similarity, with a magnitude modulated by the spring–neap cycle. Instead, the observed spatial pattern changes drastically with time, as illustrated in Fig. 15. Sometimes the spatial pattern does resemble the predicted patterns, as on 7 October (Fig. 15b) and 5 November (Fig. 15d), although the distances of the maximum energy from the ridge axis vary by  $\sim 10$  km between the two dates. However, most of the time, the observed and predicted patterns differ, as already noted for 27 September (Fig. 15a) or further illustrated for 26 October (Fig. 15c), when the area of maximum energy is located 50–70 km from the ridge axis, in an area where phase-locked  $M_2$  currents were observed to be strong (Fig. 10a), whereas phase-locked  $S_2$  currents were observed to be weak (Fig. 12a).

Such modulations of the spatial pattern of semidiurnal kinetic energy do not necessarily imply a modulation of the semidiurnal wave energy as a whole. To investigate the latter, the complex-demodulated semidiurnal kinetic energy fields observed by the HFRs were spatially averaged over the observational domain, to obtain the temporal evolution of the energy of the semidiurnal wave field at the surface (Fig. 16). The localized enhancement of energy near C1 from 24 to 30 September was partially counterbalanced by reductions of energy at other locations and did not affect much the spatially averaged energy level. At other times, however, the spatially averaged energy contained in the high-pass filtered currents substantially exceeded that contained in the phase-locked semidiurnal currents (e.g., from 12 October to 2 November 2002). Although the former was greater than the latter most of the time in fall 2002, there was a period in spring 2003 (15–24 March) when the high-pass filtered energy was weaker than the phase-locked energy. However, this was more than compensated for by a large increase of

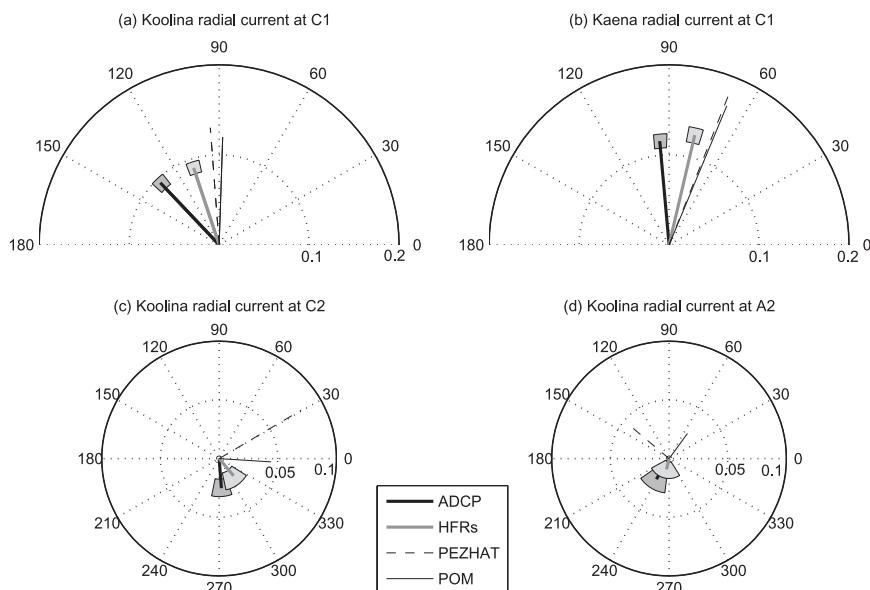


FIG. 9. Total (barotropic plus baroclinic)  $M_2$  surface radial currents in the directions from (a) Ko Olina and (b) Kaena at C1 and in the direction from Ko Olina at (c) C2 and (d) A2. The legend is as in Fig. 8. Observed current parameters were obtained from harmonic analysis on radial currents. Predicted current parameters were obtained by projecting the tidal ellipses on the radial directions. Phases are represented by the angle and amplitudes by the length of the straight lines, and 95% confidence intervals on amplitude and phase are shown by shaded areas (dark gray for ADCPs and light gray for HFRs).

high-pass-filtered energy relative to phase-locked energy during 14–25 April, so that the time-averaged energy contained in the high-pass-filtered currents was 1.3 times stronger than the time-averaged energy contained in the phase-locked semidiurnal currents during spring 2003, a level similar to that during fall 2002. This amounts to  $\sim 20\%$  of semidiurnal energy leaked into incoherent signals.

## 6. Discussion

At least two features of our observations deserve some discussion: (i) the discrepancies between observed and predicted  $M_2$  kinetic energy spatial pattern and magnitude and the dissimilarity between the observed  $M_2$  and  $S_2$  kinetic energy spatial patterns and (ii) the apparent seasonal variability of observed  $M_2$  currents.

### a. Discrepancies between observed and predicted semidiurnal currents

We showed in section 5 that the observed amplitude and phase of semidiurnal currents are modulated on time scales shorter than the spring–neap cycle. These modulations, incoherent with astronomical forcing, induced a leaking of  $\sim 20\%$  of semidiurnal kinetic energy into incoherent signals, not captured when least squares fitting tides over the 59-day records. Similar modulations

of semidiurnal internal tides have been observed elsewhere (e.g., Mogaard and McKee 1973; Huthnance and Baines 1982; Siedler and Paul 1991; Eich et al. 2004; van Haren 2004; Hosegood and van Haren 2006). Van Haren (2004) found that the incoherent signal comprised  $\sim 30\%$  of the total tidal kinetic energy in current meter observations in the Bay of Biscay, whereas Hosegood and van Haren (2006) found smaller values of 18%–20% (similar to ours) in moored ADCP observations in the Faeroe–Shetland Channel. Gerkema (2002) modeled the spring–neap cycle in the Faeroe–Shetland Channel and found that a small change in the stratification profile could lead to shifts of the time at which baroclinic spring tides occur (relative to the occurrence of barotropic spring tides) as large as a week at some positions. He concluded that “at such positions one would never expect to find a consistent spring–neap cycle since in nature, small variations in background conditions are always present.” Closer to our observational area, Eich et al. (2004) found as much as 40% of energy in semidiurnal band at frequencies other than the tidal constituents in moored current meter observations in Mamala Bay (the south shore of Oahu east of the Ko Olina HFR in Fig. 1).

Although we cannot separate the amount of energy lost by each semidiurnal constituent, if we assume that each constituent loses the same fraction of energy into incoherent signals, then  $M_2$  lost  $\sim 20\%$  of its energy. If

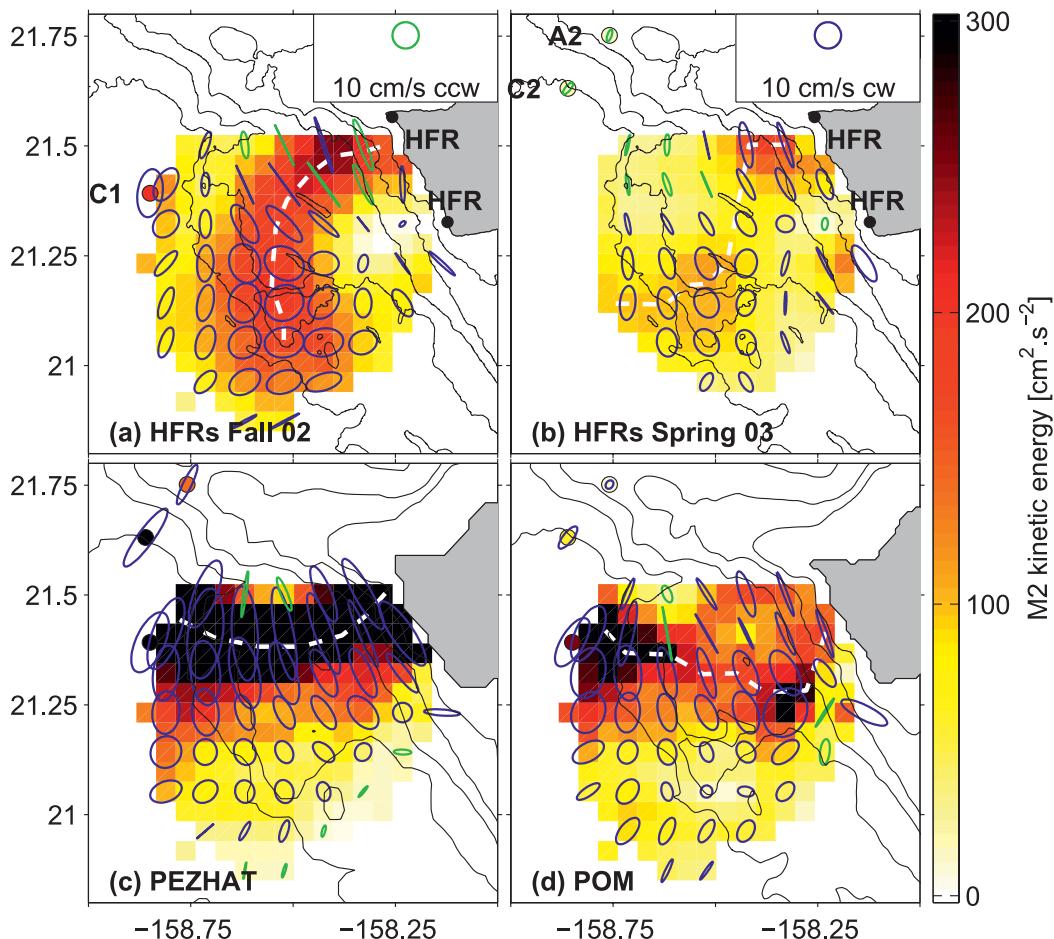


FIG. 10. Kinetic energy and current ellipses (green is counterclockwise and blue is clockwise) of total (barotropic plus baroclinic)  $M_2$  surface currents observed during (a) fall 2002 and (b) spring 2003 and predicted by (c) PEZHAT and (d) POM (smoothed over the HFR grid). The local maxima of kinetic energy are indicated by white dashed lines. Ellipses are shown every 2 grid points in longitude and latitude.

so, the actual energy contained in  $M_2$  currents should be 1.25 times higher than estimated from the phase-locked currents. This would bring the observed energy level during fall 2002 higher than predicted by POM (Table 2), consistent with a possible underestimation of internal tide energy resulting from the lack of body forcing in POM. However, the adjusted observed energy levels remain weaker than those predicted by PEZHAT, which is consistent with a possible overestimation of internal tide energy resulting from the weak mixing coefficients and lack of stress within the bottom boundary layer in PEZHAT.

An irregular spring–neap cycle does not necessarily require different spatial structures for  $M_2$  and  $S_2$ , however. These differences arise from the least squares fit analysis because of the temporal variability of the spatial structure of semidiurnal kinetic energy (Fig. 15). What mechanisms could cause such variability? In the numerical predictions, the areas of strongest energy at the surface

correspond to the positions where internal tide beams reflect from the sea surface. These beams are due to the superposition of many horizontally propagating vertical modes, which all have different horizontal wavelengths and phase speeds and therefore reach a particular position at different phases. At most positions, the modes are out of phase, leading to a weak total signal from their superposition, whereas at some particular positions all the modes are in phase, leading to a strong total signal. The resulting spatial pattern displays beams of enhanced energy (Fig. 6). In a similar way as for the spring–neap cycle variability mentioned above, if phase shifts are introduced for each vertical mode (with different values for each mode), then the beam pattern could be modified.

The simplest model to illustrate this is to consider the effect of a homogeneous barotropic background current  $U$  on the propagation of vertical modes in a nonrotating hydrostatic ocean with a flat bottom at depth  $H$  and

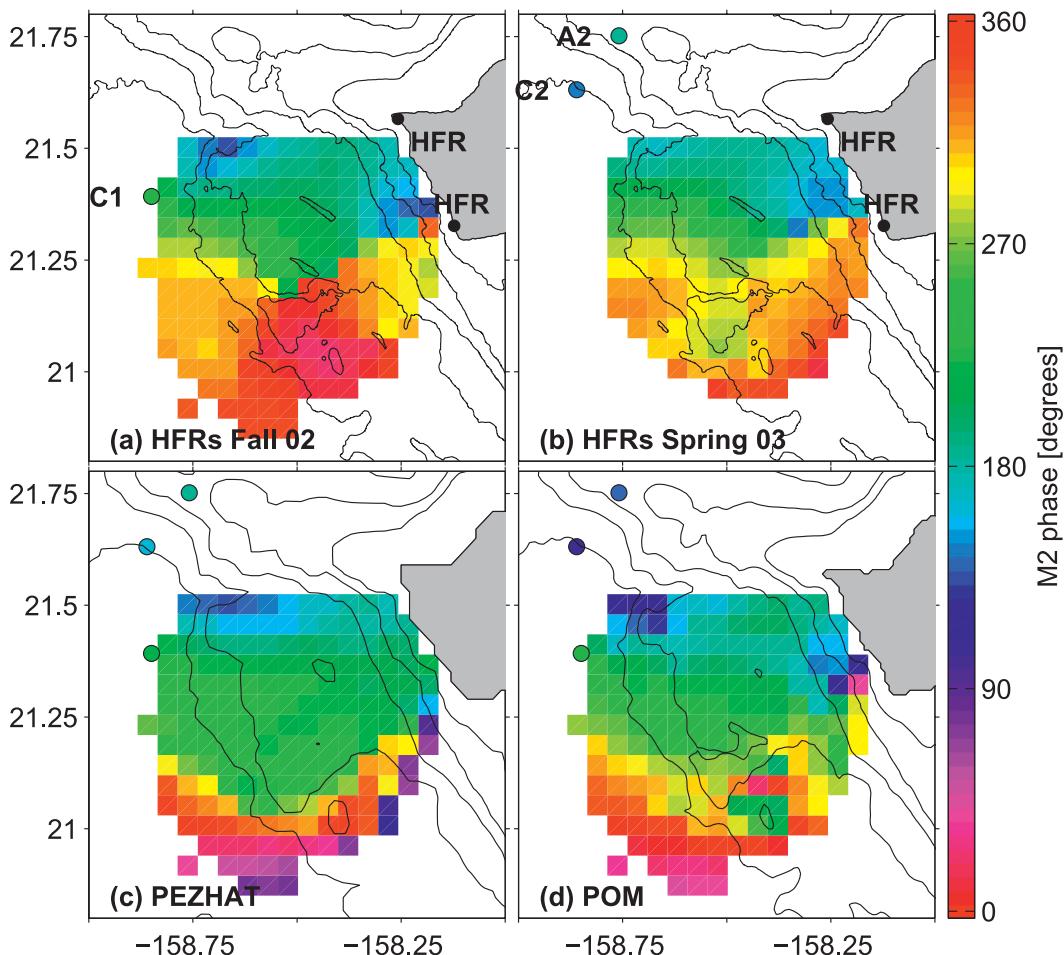


FIG. 11. As in Fig. 10, but for phase.

constant stratification  $N$ . We assume that the modes are generated at middepth at  $x = 0$  and propagate toward  $x > 0$ . We also assume the problem to be  $y$  independent. The dispersion relation for internal mode  $n$  ( $n = 1, 2, \dots$ ) is

$$\omega_n = \frac{NHk_n}{n\pi} + k_n U, \tag{4}$$

where  $\omega_n$  and  $k_n$  are the frequency and horizontal wavenumber of mode  $n$ , respectively. For tidal forcing, all modes have the same frequency (e.g.,  $\omega_n = \omega_{M_2}$ ), so their horizontal wavenumbers are

$$k_n = \frac{\omega_{M_2}}{c_n + U}, \tag{5}$$

where  $c_n = NH/n\pi$  is the phase speed of mode  $n$ . We see that the horizontal wavenumber is affected differently by the background current for different modes, depending on the ratio of phase speed  $c_n$  to background velocity  $U$ . Typically in the ocean, the phase speed of mode 1 is

$c_1 = O(1 \text{ m s}^{-1})$ , whereas barotropic subinertial currents are at least an order of magnitude smaller,  $U \leq 0.1 \text{ m s}^{-1}$ . Therefore, the wavelengths of the lowest vertical modes are barely affected by barotropic background currents, whereas those of higher vertical modes, which are necessary to produce beamlike structures, are substantially modified. As a result, beams can be strongly distorted

TABLE 2. Ratios of spatially averaged kinetic energy: upper triangle:  $M_2$  (ratios of columns to rows; e.g., HFR1 divided by HFR2 for first row, second column); lower triangle:  $S_2$  (ratios of rows to columns; e.g., HFR1 divided by HFR2 for second row, first column). HFR1 is for fall 2002 and HFR2 is for spring 2003. Kinetic energy values were averaged over the largest common area covered by each pair of datasets.

	$M_2$			
$S_2$	HFR2	HFR1	POM	PEZHAT
HFR2	1.0	1.7	1.8	3.2
HFR1	1.2	1.0	1.1	1.8
POM	1.2	1.2	1.0	1.7

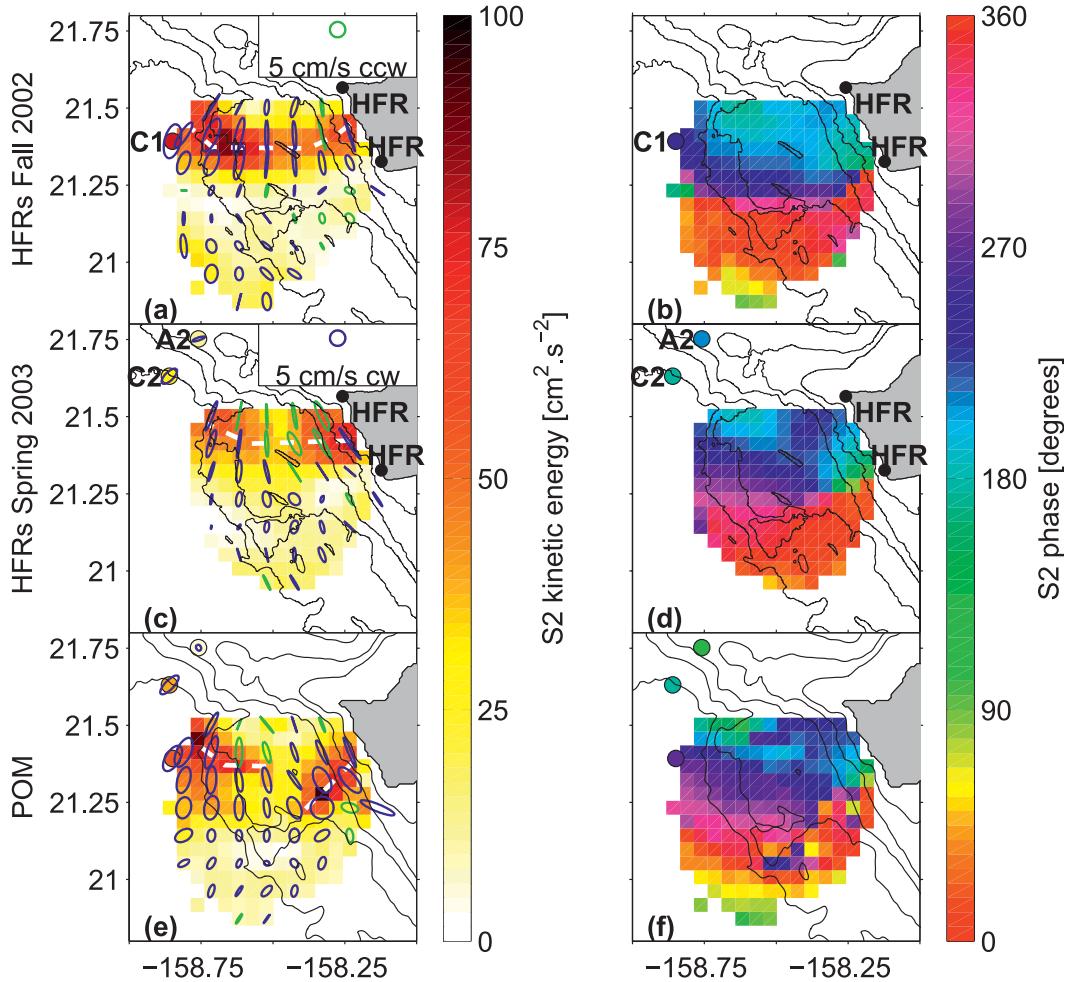


FIG. 12. (left) Kinetic energy and current ellipses (green is counterclockwise and blue is clockwise) and (right) phase of total (barotropic plus baroclinic)  $S_2$  surface currents observed during (a),(b) fall 2002 and (c),(d) spring 2003 and predicted by (e),(f) POM (smoothed over the HFR grid). The local maxima of kinetic energy are indicated by white dashed lines. Ellipses are shown every 2 grid points in longitude and latitude.

even by barotropic background currents that are much slower than the phase speed of the lowest vertical modes.

This is illustrated in Fig. 17, which shows the standard deviation of the zonal current  $u$  obtained from the summation of 20 vertical modes at  $M_2$  frequency with different background velocities,

$$u(x, z, t) = \sum_{n=1}^{n=20} n^{-1} \cos\left(\frac{n\pi z}{H}\right) \cos(k_n x - \omega_{M_2} t - n\pi/2), \quad (6)$$

where  $k_n$  is given by Eq. (5) (the phase  $-n\pi/2$  is chosen to obtain an upward-propagating beam originating at depth  $H/2$  at  $x = 0$ ). Without background current (Fig. 17a), a well-defined beam reflects from the surface 36 km from the origin (white dashed line) and subsequently bounces

back and forth between the bottom and surface. With a background current of  $5 \text{ cm s}^{-1}$  (1.5% of the first-mode phase speed) in the direction opposite to the propagation direction of the vertical modes, the beam is significantly affected (Fig. 17b); it surfaces 6.5 km closer to the origin, and energy along the beam is dispersed, especially after the first surface reflection. Surface energy averaged within  $\pm 25 \text{ km}$  from the position of maximum energy in the absence of background current (black dashed lines, mimicking the area observed by the HFRs in the Kauai Channel), is reduced by 7%. With a stronger background current of  $10 \text{ cm s}^{-1}$  (3% of the first-mode phase speed), the beam surfaces 9.5 km closer to the origin, and the average surface energy within the 50-km area is reduced by 14% (Fig. 17c). If the direction of the background current is reversed, the beam surfaces 10.5 km farther away from the origin than in the absence of background

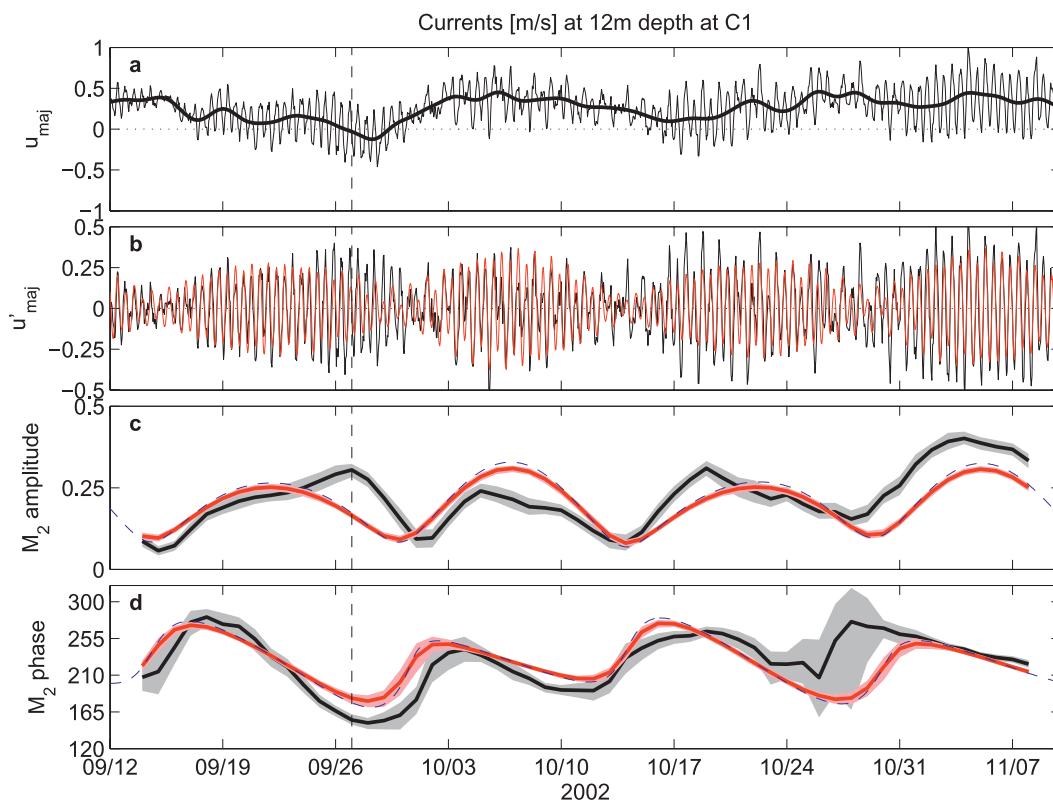


FIG. 13. (a) Currents (projected in the direction of the phase-locked  $M_2$  major axis) at 12-m depth from the upper ADCP at C1: hourly averaged (thin line) and low-pass filtered (thick line) with a 2-day cutoff period; (b) high-pass filtered currents [black line; i.e., difference between thin and thick lines in (a)] and phase-locked semidiurnal currents (red line; summing  $M_2$ ,  $S_2$  and  $N_2$  constituents); and complex-demodulated semidiurnal major axis (c) amplitude and (d) phase for the high-pass filtered (black lines) and phase-locked semidiurnal (red lines) currents. Shadings indicate 95% confidence intervals. Predictions from Eqs. (2) and (3) are shown by blue dashed lines. The vertical dashed line indicates the time of the passage of a strong mesoscale oceanic cyclone (Fig. 15a).

current (Fig. 17d); however, in this case the average surface energy within the 50-km area is increased by 11%.

This simple model suggests a plausible mechanism by which the spatial pattern of semidiurnal kinetic energy can be modified in the Kauai Channel. However, a direct correspondence between the results of the simple model (Fig. 17) and the observations (Fig. 15) cannot be established for the following reasons: (i) topography in the Kauai Channel is not flat, (ii) stratification is not constant, (iii) barotropic currents were not observed (except at A2 in spring 2003), and (iv) they are likely to be horizontally varying; furthermore, (v) background currents also have a strong baroclinic component.

Rainville and Pinkel (2006) addressed point (iv) using a horizontal ray-tracing approach and showed that vertical mode trajectories were modified by horizontally sheared background barotropic currents, with the higher modes being more strongly affected. This adds another mechanism to smear out the internal tide beam energy. However, the simple model used here or the approach

used by Rainville and Pinkel (2006) can neither deal with strongly varying topography, as found in the Kauai Channel, nor deal with baroclinic background currents, because vertical modes become coupled together in the presence of variable topography (Griffiths and Grimshaw 2007) or vertically sheared currents (Mooers 1975). A 3D ray-tracing approach is used in Part II to investigate the effects of horizontally and vertically sheared background currents on internal tides propagation. It is argued in Part II that the peculiar spatial pattern of semidiurnal kinetic energy on 27 September (Fig. 15a) could result from the impact of a mesoscale cyclone (revealed by the subinertial currents) on internal tide propagation. Similarly, the modulation of spatially averaged kinetic energy during spring 2003, with the high-pass-filtered energy weaker than the phase-locked energy during 15–24 March but stronger during 14–25 April (Fig. 16), could result from the impact of mesoscale vorticity waves on internal tide propagation. These waves had a northeastward phase propagation, and their frequency and wavenumber

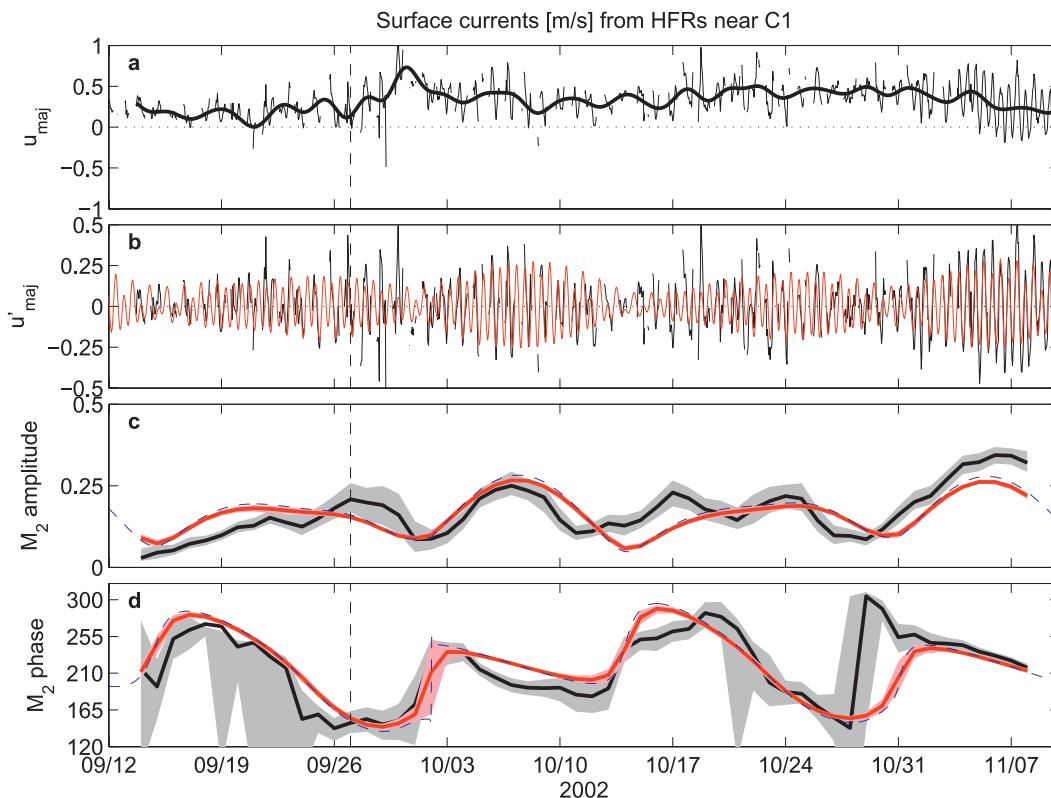


FIG. 14. As in Fig. 13, but for HFR surface currents at the grid point closest to C1.

satisfied the dispersion relation of vortex Rossby waves propagating on the radial gradient of potential vorticity associated with a large cyclone south of Kauai (Chavanne et al. 2010, manuscript submitted to *J. Phys. Oceanogr.*).

Differences between  $M_2$  and  $S_2$  spatial structures have been observed elsewhere: for example, Gould and McKee (1973) obtained different energy distributions as a function of vertical modes for  $M_2$  and  $S_2$  currents on the continental slope in the Bay of Biscay. Spatial differences in the ratio of  $M_2/S_2$  baroclinic amplitudes were observed on the Australian North West Shelf (Holloway 1984) and in the Laurentian Channel (Wang et al. 1991). In the presence of such variability, one cannot expect to obtain by least squares fit similar spatial patterns for tidal constituents closer to each other in frequency than to the inertial frequency, such as  $M_2$  and  $S_2$  in the Kauai Channel, even though their generation and propagation characteristics should be similar.

*b. Apparent seasonal variability of  $M_2$  currents*

Lower  $M_2$  kinetic energy levels were recorded in spring 2003 than in fall 2002. Similar seasonal differences were also observed by Eich et al. (2004) in Mamala Bay:  $M_2$  baroclinic currents were more energetic in summer, when the water column is highly stratified, than in winter at two

moorings on the eastern side of the bay. With the percentage of energy leaking into incoherent signals being similar for fall 2002 and spring 2003 (Fig. 16), the effects of mesoscale currents on internal tide propagation cannot explain the observed seasonal differences.

A possible candidate mechanism is the strong stratification in the seasonal thermocline observed during fall 2002 (Fig. 3a), which could partially reflect the upward-propagating internal tide beams. Gerkema (2001) studied the propagation of internal waves in an ocean with an idealized stratification consisting of a mixed upper layer and a linearly stratified lower layer, with a density jump across the interface, which represented the thermocline. He showed that, in the absence of a thermocline, the beams were reflecting off the sea surface; in the presence of a strong thermocline, they were almost entirely reflecting off the thermocline. With a moderately strong thermocline, some energy was leaking into the mixed layer. This would imply in our case that the energy reaching the surface should be stronger in spring (when the seasonal thermocline weakens; Fig. 3a) than in fall, contrary to our observations. This particular mechanism must not be dominant here.

Another possible candidate mechanism is that the barotropic to baroclinic energy conversion efficiency can be modulated by background stratification and current

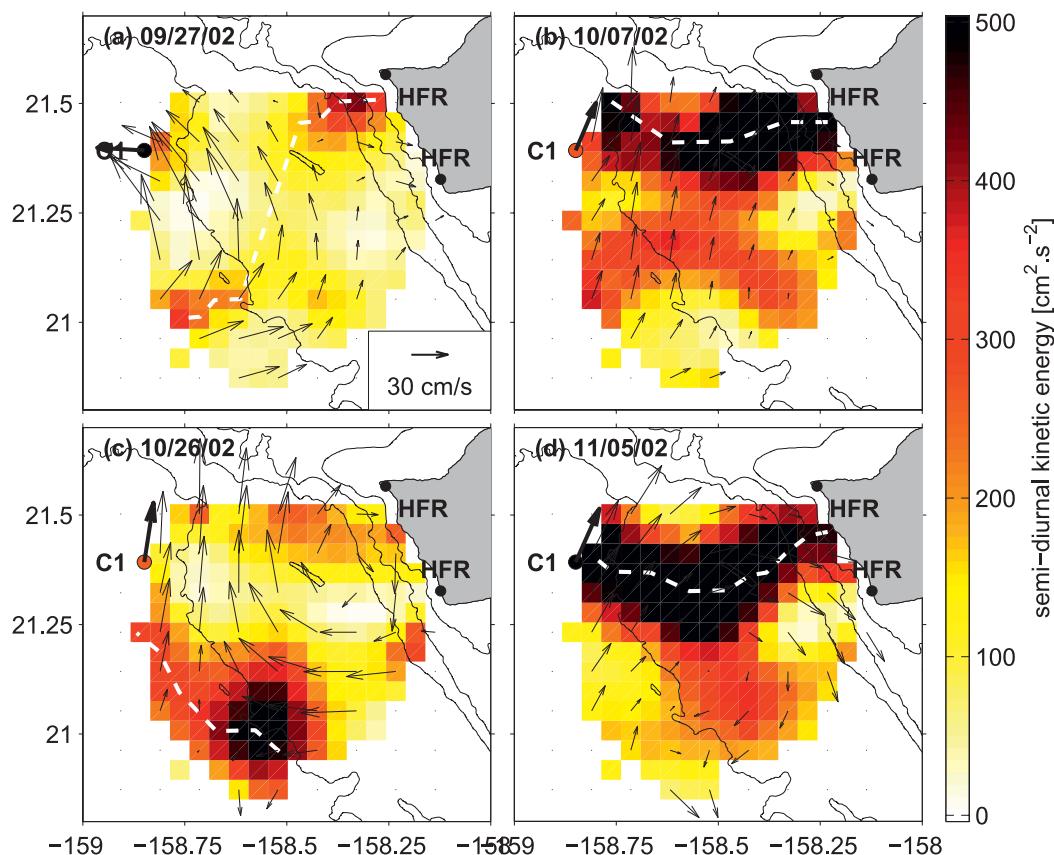


FIG. 15. Complex-demodulated semidiurnal kinetic energy from high-pass-filtered currents using 4-day windows centered on (a) 27 Sep, (b) 7 Oct, (c) 26 Oct, and (d) 5 Nov 2002. Subinertial surface currents are overlain as black vectors [scale given in (a)]. The local maxima of kinetic energy are indicated by white dashed lines.

variability. Indeed, observations at mooring A2 show that the barotropic to baroclinic  $M_2$  energy conversion rates vary on time scales on the order of a month and increased by  $\sim 50\%$  from March to April 2003 (N. Zilberman et al. 2010, unpublished manuscript), therefore possibly contributing to the stronger semidiurnal surface kinetic energy observed during the mid-April than during the mid-March spring tides (Fig. 16). N. Zilberman et al. (2010, unpublished manuscript) attribute the modulation of the energy conversion to the advection of the mode 2 internal tide by background currents, which modulates the phase of the perturbation pressure at the bottom. Unfortunately, no analyses of the energy conversion at the bottom over the ridge are available during fall 2002 to confirm whether this mechanism could explain the difference in energy levels between fall 2002 and spring 2003.

## 7. Conclusions and broader implications

Observations of currents by high-frequency radio Doppler surface current meters and moored ADCPs

south of Kaena Ridge, in the Kauai Channel, Hawaii, show that superinertial variability is dominated by semidiurnal tides. Phase-locked  $M_2$  and  $S_2$  currents, extracted by least squares fits over two 59-day periods in fall 2002 and spring 2003, were compared with numerical predictions from two 3D high-resolution models of the tides, which showed that, over the observed area, semidiurnal surface currents are dominated by the baroclinic modes. The observed and predicted phase patterns are in good agreement for both  $M_2$  and  $S_2$  currents, showing southwestward propagation of internal tides away from their generation locations on the ridge flanks. The observed and predicted kinetic energy patterns are in good agreement for  $S_2$ , showing a band of enhanced energy between 30 and 40 km from the ridge axis, corresponding to the first surface reflection of internal tide beams emanating from critical slopes on the northern ridge flank. Although the predicted  $M_2$  pattern is similar (but stronger in amplitude) to the predicted  $S_2$  pattern, the observed  $M_2$  pattern is quite different from the observed  $S_2$  pattern: the area of enhanced energy corresponding to the first

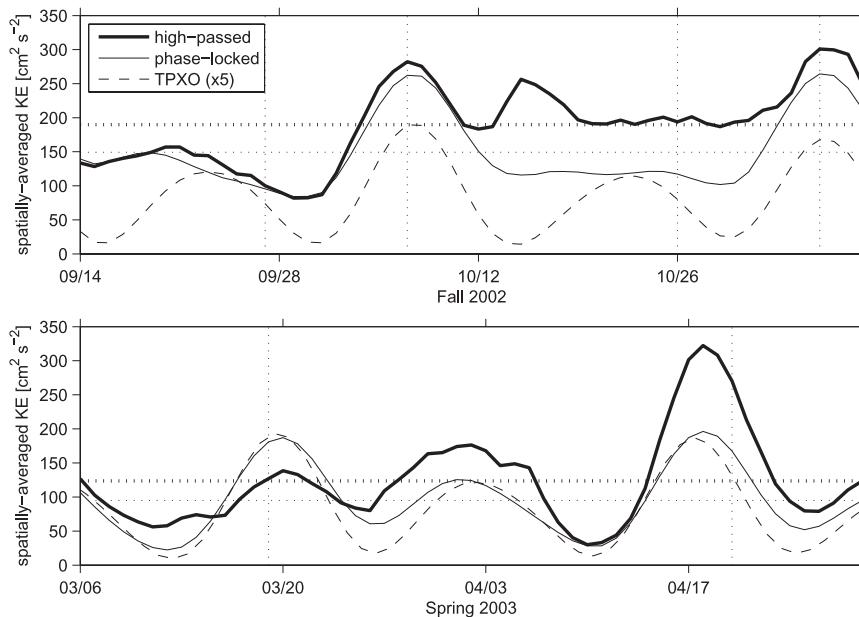


FIG. 16. Time series of complex-demodulated semidiurnal kinetic energy, spatially averaged over the observational domain, during (a) fall 2002 and (b) spring 2003, from high-pass filtered (thick solid lines) and phase-locked semidiurnal (thin solid lines) currents. Their temporal averages are shown by horizontal dotted lines. For comparison with barotropic forcing, complex-demodulated semidiurnal (summing  $M_2$ ,  $S_2$ ,  $N_2$ , and  $K_2$  constituents) barotropic kinetic energy predicted by TPXO (Egbert and Erofeeva 2002), averaged over the rectangular area indicated in Fig. 4a, is shown by thin dashed lines (kinetic energy values have been multiplied by a factor of 5 for clarity). Vertical dotted lines indicate the times of the snapshots shown in Fig. 15 during fall 2002 and the snapshots of vorticity waves shown in Part II during spring 2003.

surface reflection of  $M_2$  beams is observed 10–20 km farther away from the ridge and with weaker magnitude than predicted.

Complex demodulation of the semidiurnal currents reveals a strong temporal variability in the spatial pattern and amplitude of kinetic energy. Part of this variability is due to interferences between the semidiurnal constituents (e.g., spring–neap cycle), but part of the variability is incoherent with astronomical forcing and amounts to  $\sim 20\%$  of total semidiurnal kinetic energy. We propose that the incoherent variability could be due to the effects of variable background currents and stratification on internal tide propagation. For example, a barotropic background current flowing parallel to the direction of the internal tide propagation will induce a Doppler shift proportional to the horizontal wavenumber of each vertical mode and to the distance from their generation location. As a result, internal tide beams, which require a coherent superposition of many vertical modes, are smeared out by barotropic background currents as weak as a few percents of the first-mode phase speed, and their first surface reflection location is shifted significantly. Kinetic energy spatial pattern and amplitude modulations incoherent with the spring–neap cycle

lead to different structures for phase-locked  $M_2$  and  $S_2$  currents extracted by least squares fits.

These results have potentially important implications for estimations of tidal energy budgets from observations. The fast barotropic tide is negligibly affected by mesoscale variability; therefore, the energy lost from the barotropic tides is well constrained by models assimilating satellite observations (Egbert and Ray 2000, 2001; Zaron and Egbert 2006a). The slower internal tides, however, can be substantially affected by mesoscale variability, so that a significant amount of energy is smeared into incoherent signals. Therefore, estimations of baroclinic energy fluxes from assimilations of phase-locked satellite observations should be considered as lower bounds (Ray and Cartwright 2001; Dushaw 2002), due in part to the incoherent energy not captured by the altimeters. However, the baroclinic energy fluxes radiating away from the Hawaiian Ridge are dominated by the lowest vertical modes (Merrifield and Holloway 2002; St. Laurent and Nash 2004), which are only weakly affected by mesoscale variability close to the ridge (Rainville and Pinkel 2006). Therefore, baroclinic energy flux estimates from altimetry observations are not expected to be too sensitive to stratification variability (Dushaw

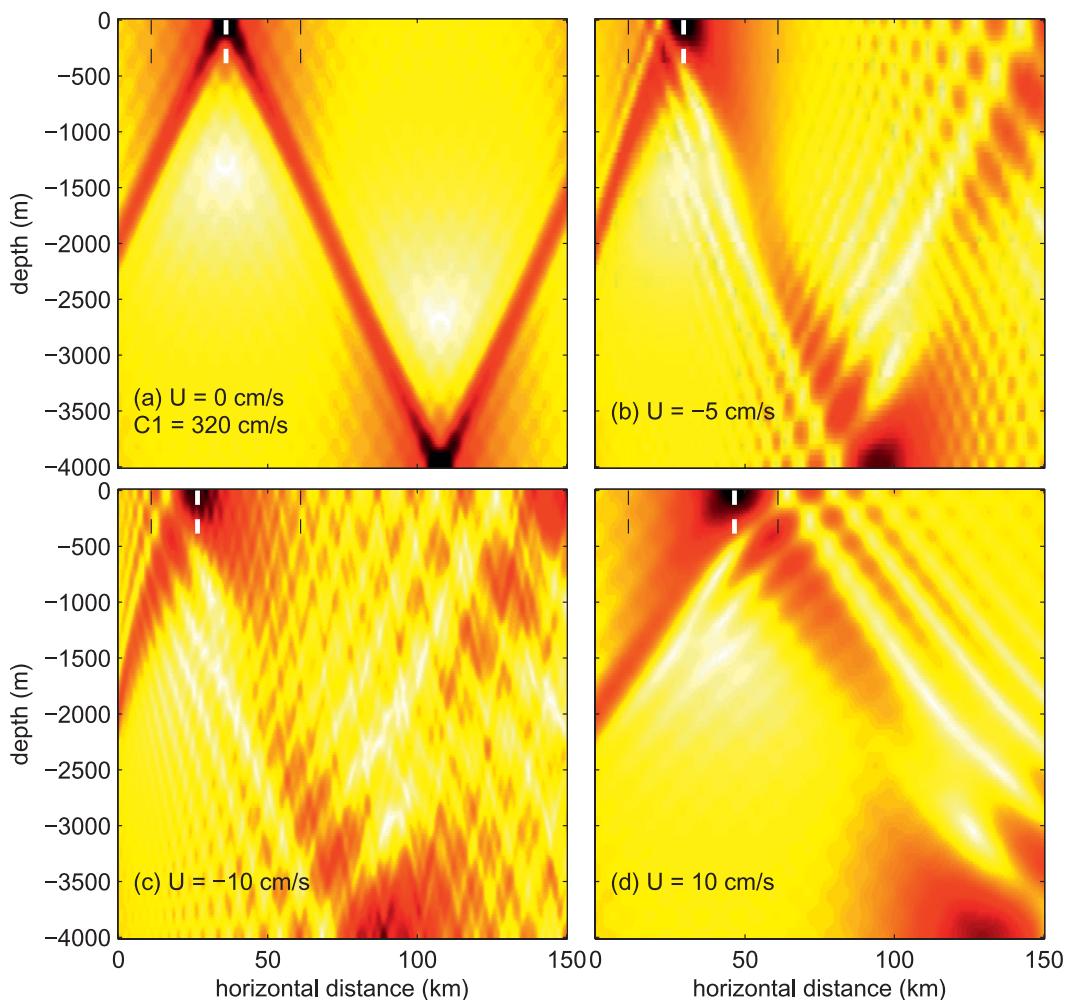


FIG. 17. Superposition of 20 vertical modes at  $M_2$  frequency in a nonrotating hydrostatic ocean with a flat bottom (4000 m deep) and constant stratification, in the presence of a uniform barotropic background current  $U$ : (a)  $U = 0 \text{ cm s}^{-1}$ , (b)  $U = -5 \text{ cm s}^{-1}$ , (c)  $U = -10 \text{ cm s}^{-1}$ , and (d)  $U = 10 \text{ cm s}^{-1}$ . A negative value for  $U$  indicates that the current is flowing opposite to the direction of propagation of the modes. The phase speed of the first vertical mode is  $320 \text{ cm s}^{-1}$ , similar to that for the Kauai Channel (Zaron et al. 2009). Colors show the standard deviation of currents over one tidal period (same arbitrary scaling for each panel). White dashed lines show the locations of the first surface maximum of energy. Black dashed lines show an area of  $\pm 25 \text{ km}$  centered on the location of the first surface maximum of energy in the absence of background currents, mimicking the area covered by the HFRs in the Kauai Channel.

2002). Nevertheless, Zaron et al. (2009) assimilated the phase-locked  $M_2$  radial currents observed by the HFRs into PEZHAT and obtained a 25% reduction in the  $M_2$  baroclinic conversion rate averaged over their model domain, relative to the predictions without data assimilation. This demonstrates that assimilating phase-locked observations can lead to a substantial underestimation of baroclinic energy fluxes. Finally, dissipation of baroclinic tidal energy could be affected by the interaction between internal tides and background currents, as discussed in Part II, prompting the

need to include mesoscale currents into numerical simulations of the tides.

*Acknowledgments.* The authors thank Eric Firing and Theo Gerkema for fruitful scientific discussions. The comments of two anonymous reviewers contributed to improve the manuscript. Olivier Ali, François Ascani, Jérôme Aucan, Pierre Balmas, Camille Bandet, Marion Bandet, Joël Benito, Marie-Stéphanie Bour, Thomas Decloedt, Julie Degoulet, Sophie Delambert, Julie Deshayes, Adrien Desoria, Bénédicte Dousset, Pierre

Dutrieux, Tania Dutrieux, Yvonne Firing, Io Flament, Maël Flament, Monika Hamann, Thomas Helzel, Matthias Kniephoff, Oliver Koshe, Kimball Millikan, Philip Moravcik, Mitch Pinkerton and Derek Young helped with radar installation and maintenance, and with data processing. HFR processing routines by Jeff Paduan and Mike Cook were adapted to compute vector currents from radial measurements. Administrative assistance was provided by Laura Glenn and Lance Samura. We are grateful to the following individuals and institutions for providing permits and for helping with logistics: Ko Olina: Ko Olina Resort and Marina, Honolulu; Jack Morgan and Ken Williams; Kaena: Kaena Point Satellite Tracking Station; Kristopher Breaux, Lance Hayashi and Roy Shigemura. Support was obtained from National Science Foundation Grants OCE-9724464, OCE-0426112, and OCE-0453848 to P. Flament; OCE-0425347 to M. Merrifield; OCE-9819533 to D. Luther; OCE-9819532 to M. Levine and T. Boyd; and OCE-9819518 and OCE-0623540 to G. Edgbert and E. Zaron. The Hawaii Ocean Time Series is supported by NSF Grant OCE-0327513. P. Flament, M. Merrifield and D. Luther are also supported by the State of Hawaii. This publication was prepared under cooperative Agreement NA07NOS4730207 from the National Oceanographic and Atmospheric Administration Integrated Ocean Observing System Program Office, U.S. Department of Commerce.

## APPENDIX A

### Instrument Settings and Data Processing

The frequency-modulated continuous-wave (FMCW) HFRs were operated with 100–125-kHz bandwidth, yielding a range resolution of 1.2–1.5 km. A chirp length of 0.26–0.34 s, averaging time of 9–12 min, and repeat cycles of 20–30 min were programmed, with each site transmitting while the other was quiet. The transmit antenna arrays formed a beam toward the ocean, a null in the direction of the receive antennas to reduce the direct path energy, and a 22-dB rejection of the back signal (critical at Kaena Point to attenuate the echoes from the northern side of the Kauai Channel). The instruments were operated in beam-forming mode with linear arrays of 16 receive antennas, oriented at 302° clockwise from north at Kaena and 355° at Ko Olina, yielding an azimuthal resolution of  $\sim 7^\circ$  when steering the beam normal to the receive array and degrading at higher incidence angles; above 60° the sidelobes are too large to obtain uncontaminated measurements (Gurgel et al. 1999).

The maximum range of good measurements depends on the signal propagation conditions and on the ambient

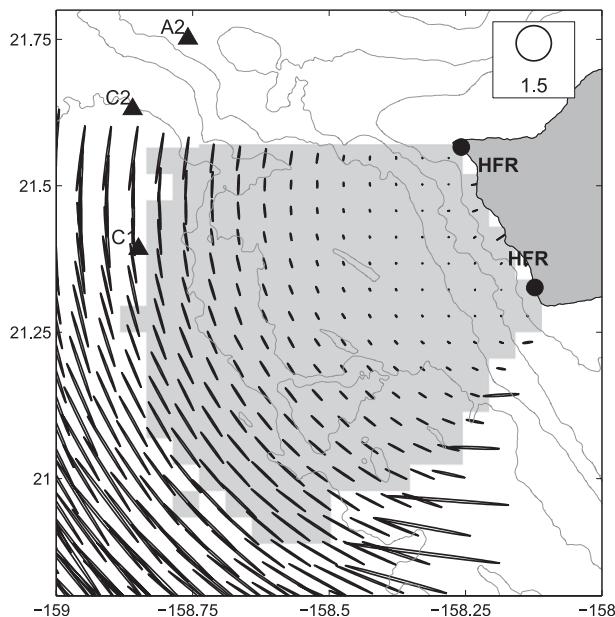


FIG. A1. GDOP ellipses: The legend corresponds to the threshold value selected to discard vector currents poorly constrained. The area of 50% data return for vector currents is shaded in light gray. Moorings are indicated by black triangles and HFRs are indicated by black bullets.

electromagnetic noise. During the experiment, there was a marked diurnal modulation of coverage (Fig. 1). The maximum day (night) ranges of 50% data return were 121 km (94 km) for Ko Olina, and 127 km (103 km) for Kaena from September to November 2002. Presumably, the D layer of the ionosphere, which is more dissipative, inhibits the propagation of distant electromagnetic signals in daytime but disappears at night, leaving the more reflective E layer to propagate distant electromagnetic noise. To reduce the impact of this modulation on the analysis of tidal constituents, least squares fits were performed only if more than half of the data were available. It should be noted that  $M_2$  will be less affected by a diurnal modulation of data availability than  $K_1$  (separated from  $S_1$  by only one cycle per year) or  $S_2$ .

Vector currents were mapped on a 5-km resolution Cartesian grid by least squares fitting the zonal and meridional components to radial measurements from both sites within a 5-km search radius. A major problem is the geometric dilution of precision (GDOP), which amplifies measurement errors when the angles between the different radial directions available are close to 0° or 180°. Following Chavanne et al. (2007), we use the principal axes of the covariance matrix of the vector currents, shown in Fig. A1, to discard poorly constrained estimates when the major axis amplitude exceeded 1.5.

Upward-looking 300-kHz ADCPs were deployed at  $\sim 90$ -m depths on each mooring, providing good data up

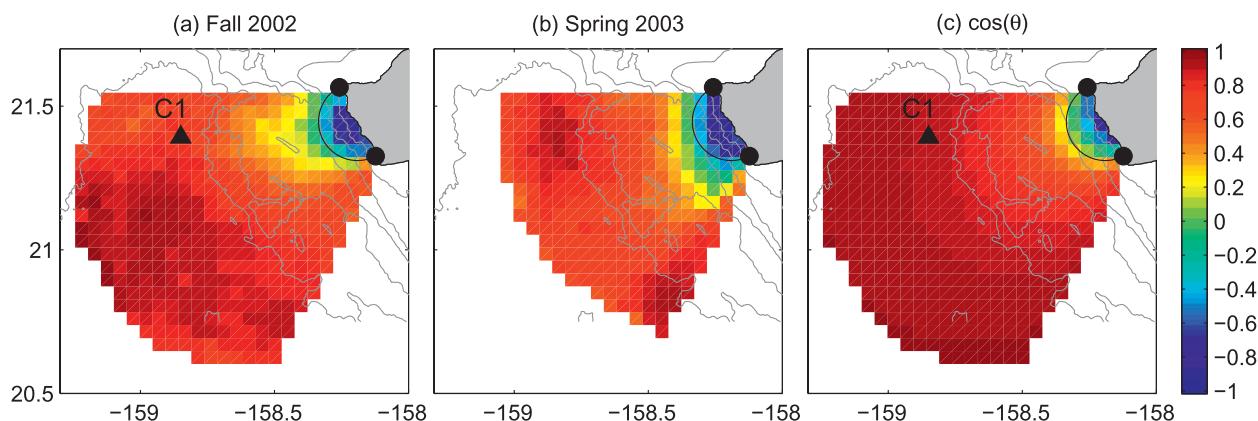


FIG. B1. Correlation between Ko Olina and Kaena radial currents for (a) fall 2002 and (b) spring 2003 and (c) the cosine of the angle between radials from the two sites. The circle where this angle is  $90^\circ$  is shown for reference (thin black line).

to 12 m below the surface, with vertical resolution of 4 m, and 10-min acquisitions at C1 and 20-min acquisitions at C2 and A2. Upward-looking 75-kHz ADCPs were deployed at  $\sim 750$ -m depths on each mooring with another one at  $\sim 1300$  m on A2, with vertical resolution of 8 m, and 8-min acquisitions at C1, 10-min acquisitions at C2, and 16-min acquisitions at A2. The two deepest ADCP ranges at A2 were overlapping for a few depth bins. Visual inspection of the data prompted us to discard the middle ADCP data in favor of the deepest ADCP where they overlapped. At all moorings, there were diurnally missing observations between 160 and 350 m because of a lack of scatterers, mostly during daytime (with a peak of missing data around 1000 local time), presumably because of the diel vertical migration of zooplankton.

Tides are extracted by least squares fit, which minimizes the sum of the squares of differences between the data and the model function (here a constant plus sines and cosines at tidal frequencies). Because of the squaring, more weight is given to large departures of the data from the model function than to small departures. Large departures could be due to strong low-frequency currents superimposed on tidal currents. To avoid low-frequency currents biasing the least squares fit estimates, the currents are high-pass-filtered before tides are extracted. Time series with missing data are handled as follows: the strong semidiurnal  $M_2$  tide was first removed by successive least squares fits over a 2-day sliding window to reduce spectral leakage into lower frequencies. Small data gaps were then linearly interpolated, and the residual currents were low passed by a 44-step finite impulse response filter, run forward and backward, with a 2-day cutoff period. The low-passed currents were then subtracted from the original observations (retaining the missing data structure) to obtain the high-pass-filtered

currents. Tidal fits were then performed only if less than 50% of data were missing. Uncertainties are estimated by a bootstrap technique: the tides estimated by least squares fit are removed from the high-pass filtered currents to obtain time series of residual currents, or noise; 300 synthetic noise realizations are generated by randomly resampling the time series of residual currents. The tides are then added back to each noise realization, from which a new tide estimate is obtained by least squares fit. Then, 95% confidence intervals on the tidal parameters are obtained from histograms of the 300 realizations.

## APPENDIX B

### Data Validation

Because each HFR is an independent instrument, the quality of the radial currents can be assessed by the correlation between radial currents from both sites, which should approach  $-1$  along the baseline joining the two sites, where the radials are in opposite directions, and  $+1$  far offshore, where the radials are almost colinear. If along-baseline and across-baseline current components were uncorrelated with equal variance, the correlation pattern would follow that of the cosine of the angle between radials from the two sites (Chavanne et al. 2007). This is indeed well verified (Fig. B1), although the correlation is slightly lower at far ranges north of C1 than south during fall 2002 and in the middle of the sector during spring 2003. This is therefore more likely attributable to the violation of the assumptions above than to measurement errors (which should increase toward the edges of the azimuthal sectors).

Scatterplots of currents observed by the ADCPs at 12-m depth and by the HFRs at the grid point closest to the moorings are shown in Fig. B2. Correlations range

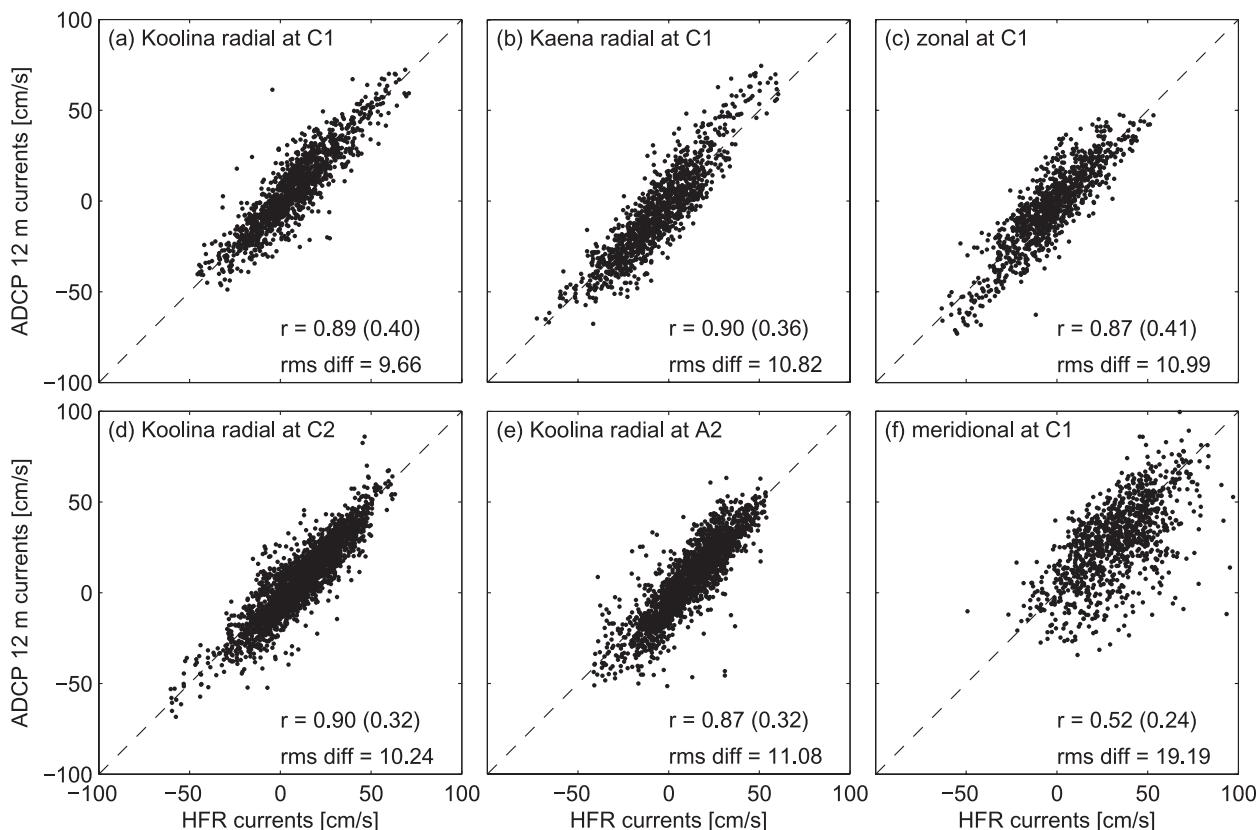


FIG. B2. Scatterplots of ADCP (ordinates) vs HFR (abscissas) currents ( $\text{cm s}^{-1}$ ). ADCP currents are from the 12-m depth bin. HFR currents are from the grid point closest to each mooring location. At C1, ADCP currents are projected in the directions from (a) Ko Olina and (b) Kaena and compared with the HFR radial currents. In addition, the (c) zonal and (f) meridional current components are compared. At (d) C2 and (e) A2, ADCP currents are projected in the directions from Ko Olina and compared to the Ko Olina HFR radial currents. Correlations ( $r$ ; the numbers in parentheses indicate the 95% confidence null hypothesis values) and rms differences are indicated in the bottom-right corners.

from 0.87 to 0.90 and root-mean-square (rms) differences range from 9.7 to 11.1  $\text{cm s}^{-1}$  for the radial currents and the zonal currents at C1. In contrast, the correlation drops to 0.52 (still significant at 95% confidence level) and the rms difference jumps to 19.2  $\text{cm s}^{-1}$  for the meridional currents at C1, illustrating the GDOP effect (Fig. A1). The threshold on GDOP major axis amplitude of 1.5 was chosen so that the area of vector currents did not extend beyond C1. Observations from both instruments are fairly consistent with each other, given their different footprints and measurement depths.

#### REFERENCES

- Alford, M. H., 2003: Redistribution of energy available for ocean mixing by long-range propagation of internal waves. *Nature*, **423**, 159–162.
- , and Z. Zhao, 2007: Global patterns of low-mode internal-wave propagation. Part I: Energy and energy flux. *J. Phys. Oceanogr.*, **37**, 1829–1848.
- , M. C. Gregg, and M. A. Merrifield, 2006: Structure, propagation, and mixing of energetic baroclinic tides in Mamala Bay, Oahu, Hawaii. *J. Phys. Oceanogr.*, **36**, 997–1018.
- , J. A. MacKinnon, Z. Zhao, R. Pinkel, J. Klymak, and T. Peacock, 2007: Internal waves across the Pacific. *Geophys. Res. Lett.*, **34**, L24601, doi:10.1029/2007GL031566.
- Boyd, T., M. D. Levine, S. R. Gard, and W. Waldorf, 2005: Mooring observations from the Hawaiian Ridge: August 2002–June 2003. OSU College of Oceanic and Atmospheric Sciences Tech. Rep. 2005-1, Data Rep. 197, 232 pp.
- Carter, G. S., and Coauthors, 2008: Energetics of  $M_2$  barotropic-to-baroclinic tidal conversion at the Hawaiian Islands. *J. Phys. Oceanogr.*, **38**, 2205–2223.
- Chavanne, C., I. Janeković, P. Flament, P.-M. Poulain, M. Kuzmić, and K.-W. Gurgel, 2007: Tidal currents in the northwestern Adriatic: High-frequency radio observations and numerical model predictions. *J. Geophys. Res.*, **112**, C03S21, doi:10.1029/2006JC003523.
- , P. Flament, D. Luther, and K.-W. Gurgel, 2010a: The surface expression of semidiurnal internal tides near a strong source at Hawaii. Part II: Interactions with mesoscale currents. *J. Phys. Oceanogr.*, **40**, 1180–1200.

- , —, and K.-W. Gurgel, 2010b: Interactions between a sub-mesoscale anticyclonic vortex and a front. *J. Phys. Oceanogr.*, in press.
- Chiswell, S. M., 2002: Energy levels, phase, and amplitude modulation of the baroclinic tide off Hawaii. *J. Phys. Oceanogr.*, **32**, 2640–2651.
- Colosi, J. A., and W. Munk, 2006: Tales of the venerable Honolulu tide gauge. *J. Phys. Oceanogr.*, **36**, 967–996.
- Cummins, P. F., J. Y. Cherniawski, and M. G. G. Foreman, 2001: North Pacific internal tides from the Aleutian Ridge: Altimeter observations and modelling. *J. Mar. Res.*, **59**, 167–191.
- Dushaw, B. D., 2002: Mapping low-mode internal tides near Hawaii using TOPEX/POSEIDON altimeter data. *Geophys. Res. Lett.*, **29**, 1250, doi:10.1029/2001GL013944.
- , B. D. Cornuelle, P. F. Worcester, B. M. Howe, and D. S. Luther, 1995: Barotropic and baroclinic tides in the central North Pacific Ocean determined from long-range reciprocal acoustic transmissions. *J. Phys. Oceanogr.*, **25**, 631–647.
- Eakins, B. W., J. E. Robinson, T. Kanamatsu, J. Naka, J. R. Smith, E. Takahashi, and D. A. Clague, 2003: Hawaii's volcanoes revealed. U.S. Geological Survey Geological Investigations Series Map I-2809.
- Egbert, G. D., and R. D. Ray, 2000: Significant dissipation of tidal energy in the deep ocean inferred from satellite altimeter data. *Nature*, **405**, 775–778.
- , and —, 2001: Estimates of  $M_2$  tidal energy dissipation from TOPEX/Poseidon altimeter data. *J. Geophys. Res.*, **106** (C10), 22 475–22 502.
- , and S. Y. Erofeeva, 2002: Efficient inverse modeling of barotropic ocean tides. *J. Atmos. Oceanic Technol.*, **19**, 183–204.
- Eich, M. L., M. A. Merrifield, and M. H. Alford, 2004: Structure and variability of semidiurnal internal tides in Mamala Bay, Hawaii. *J. Geophys. Res.*, **109**, C05010, doi:10.1029/2003JC002049.
- Flament, P., R. Lumpkin, J. Tournadre, and L. Armi, 2001: Vortex pairing in an unstable anticyclonic shear flow: Discrete subharmonics of one pendulum day. *J. Fluid Mech.*, **440**, 401–409.
- Foreman, M. G. G., 1978: Manual for tidal currents analysis and prediction. Institute of Ocean Sciences Pacific Marine Science Tech. Rep. 78-6, 57 pp.
- Gerkema, T., 2001: Internal and interfacial tides: Beam scattering and local generation of solitary waves. *J. Mar. Res.*, **59**, 227–255.
- , 2002: Application of an internal tide generation model to baroclinic spring-neap cycles. *J. Geophys. Res.*, **107**, 3124, doi:10.1029/2001JC001177.
- Gould, W. J., and W. D. McKee, 1973: Vertical structure of semidiurnal tidal currents in the Bay of Biscay. *Nature*, **244**, 88–91.
- Griffiths, S. D., and R. H. J. Grimshaw, 2007: Internal tide generation at the continental shelf modeled using a modal decomposition: Two-dimensional results. *J. Phys. Oceanogr.*, **37**, 428–451.
- Gurgel, K.-W., G. Antonischki, H.-H. Essen, and T. Schlick, 1999: Wellen Radar (WERA): A new ground-wave HF radar for ocean remote sensing. *Coastal Eng.*, **37**, 219–234.
- Holloway, P. E., 1984: On the semidiurnal internal tide at a shelf-break region on the Australian North West Shelf. *J. Phys. Oceanogr.*, **14**, 1787–1799.
- Hosegood, P., and H. van Haren, 2006: Sub-inertial modulation of semi-diurnal currents over the continental slope in the Faeroe-Shetland Channel. *Deep-Sea Res.*, **53**, 627–655.
- Huthnance, J. M., and P. G. Baines, 1982: Tidal currents in the northwest African upwelling region. *Deep-Sea Res.*, **29**, 285–306.
- Karl, D. M., and R. Lukas, 1996: The Hawaii Ocean Time-series (HOT) program: Background, rationale and field implementation. *Deep-Sea Res.*, **43**, 129–156.
- Kuhlbrodt, T., A. Griesel, M. Montoya, A. Levermann, M. Hofmann, and S. Rahmstorf, 2007: On the driving processes of the Atlantic meridional overturning circulation. *Rev. Geophys.*, **45**, RG2001, doi:10.1029/2004RG000166.
- Lamb, K. G., 2004: Nonlinear interaction among internal wave beams generated by tidal flow over supercritical topography. *Geophys. Res. Lett.*, **31**, L09313, doi:10.1029/2003GL019393.
- Larsen, J. C., 1977: Cotidal charts for the Pacific Ocean near Hawaii using f-plane solutions. *J. Phys. Oceanogr.*, **7**, 100–109.
- Ledwell, J. R., E. T. Montgomery, K. L. Polzin, L. C. S. Laurent, R. W. Schmitt, and J. M. Toole, 2000: Evidence for enhanced mixing over rough topography in the abyssal ocean. *Nature*, **403**, 179–182.
- Lueck, R. G., and T. D. Mudge, 1997: Topographically induced mixing around a shallow seamount. *Science*, **276**, 1831–1833.
- Lumpkin, R., 1998: Eddies and currents of the Hawaiian Islands. Ph.D. thesis, University of Hawaii at Manoa, 281 pp.
- Magaard, L., and W. D. McKee, 1973: Semi-diurnal tidal currents at 'site D'. *Deep-Sea Res.*, **20**, 997–1009.
- Merrifield, M. A., and P. E. Holloway, 2002: Model estimates of  $M_2$  internal tide energetics at the Hawaiian Ridge. *J. Geophys. Res.*, **107**, 3179, doi:10.1029/2001JC000996.
- , —, and T. M. S. Johnston, 2001: The generation of internal tides at the Hawaiian Ridge. *Geophys. Res. Lett.*, **28**, 559–562.
- Mooers, C. N. K., 1975: Several effects of a baroclinic current on the cross-stream propagation of inertial-internal waves. *Geophys. Fluid Dyn.*, **6**, 242–275.
- Munk, W., and C. Wunsch, 1998: Abyssal recipes II: Energetics of tidal and wind mixing. *Deep-Sea Res.*, **45**, 1977–2010.
- Pacanowski, R. C., and S. M. Griffies, 1999: The MOM3 manual. NOAA/Geophysical Fluid Dynamics Laboratory Tech. Rep., 580 pp.
- Park, J.-H., and D. R. Watts, 2006: Internal tides in the southwestern Japan/East Sea. *J. Phys. Oceanogr.*, **36**, 22–34.
- Patzert, W. C., 1969: Eddies in Hawaiian waters. University of Hawaii at Manoa Hawaiian Institute of Geophysics Tech. Rep. 69-8, 51 pp.
- Pinkel, R., and D. Rudnick, 2006: Editorial. *J. Phys. Oceanogr.*, **36**, 965–966.
- Polzin, K. L., J. M. Toole, J. R. Ledwell, and R. W. Schmitt, 1997: Spatial variability of turbulent mixing in the abyssal ocean. *Science*, **276**, 93–96.
- Qiu, B., D. A. Koh, C. Lumpkin, and P. Flament, 1997: Existence and formation mechanism for the North Hawaiian Ridge Current. *J. Phys. Oceanogr.*, **27**, 431–444.
- Rainville, L., and R. Pinkel, 2006: Propagation of low-mode internal waves through the ocean. *J. Phys. Oceanogr.*, **36**, 1220–1236.
- Ray, R. D., and G. T. Mitchum, 1996: Surface manifestation of internal tides generated near Hawaii. *Geophys. Res. Lett.*, **23**, 2101–2104.
- , and —, 1997: Surface manifestation of internal tides in the deep ocean: Observations from altimetry and island gauges. *Prog. Oceanogr.*, **40**, 135–162.

- , and D. E. Cartwright, 2001: Estimates of internal tide energy fluxes from Topex/Poseidon altimetry: Central North Pacific. *Geophys. Res. Lett.*, **28**, 1259–1262.
- Rudnick, D. L., and Coauthors, 2003: From tides to mixing along the Hawaiian Ridge. *Science*, **301**, 355–357.
- Siedler, G., and U. Paul, 1991: Barotropic and baroclinic tidal currents in the eastern basins of the North Atlantic. *J. Geophys. Res.*, **96** (C12), 22 259–22 271.
- St. Laurent, L. C., and C. Garrett, 2002: The role of internal tides in mixing the deep ocean. *J. Phys. Oceanogr.*, **32**, 2882–2899.
- , and J. D. Nash, 2004: An examination of the radiative and dissipative properties of deep ocean internal tides. *Deep-Sea Res.*, **51**, 3029–3042.
- , and H. Simmons, 2006: Estimates of power consumed by mixing in the ocean interior. *J. Climate*, **19**, 4877–4890.
- Stewart, R. H., and J. W. Joy, 1974: HF radio measurements of surface currents. *Deep-Sea Res.*, **21**, 1039–1049.
- van Haren, H., 2004: Incoherent internal tidal currents in the deep ocean. *Ocean Dyn.*, **54**, 66–76.
- Wang, J., R. G. Ingram, and L. A. Mysak, 1991: Variability of internal tides in the Laurentian Channel. *J. Geophys. Res.*, **96** (C9), 16 859–16 875.
- Wunsch, C., and R. Ferrari, 2004: Vertical mixing, energy, and the general circulation of the oceans. *Annu. Rev. Fluid Mech.*, **36**, 281–314.
- Zaron, E. D., and G. D. Egbert, 2006a: Estimating open-ocean barotropic tidal dissipation: The Hawaiian Ridge. *J. Phys. Oceanogr.*, **36**, 1019–1035.
- , and —, 2006b: Verification studies for a z-coordinate primitive-equation model: Tidal conversion at a mid-ocean ridge. *Ocean Modell.*, **14**, 257–278.
- , C. Chavanne, G. D. Egbert, and P. Flament, 2009: Baroclinic tidal generation in the Kauai Channel inferred from high-frequency radio Doppler current meters. *Dyn. Atmos. Oceans*, **48**, 93–120.